JAN 24 1986

208-C-2 C55.13/2:ERL WPL-128

NOAA Technical Memorandum ERL WPL-128

COMPLETED
65.

ORIGINAL

A FEASIBILITY STUDY ON THE USE OF FIREFINDER RADAR FOR WIND PROFILING

R. G. Strauch
A. S. Frisch
R. A. Kropfli
B. L. Weber

Wave Propagation Laboratory
Boulder, Colorado
December 1985

FOR OFFICIAL DISTRIBUTION

noaa NATIONAL OCEANIC AND ATMOSPHERIC ADMINISTRATION / Environmental Research Laboratories

BEST COPY AVAILABLE

NOAA Technical Memorandum ERL WPL-128

A FEASIBILITY STUDY ON THE USE OF FIREFINDER RADAR FOR WIND PROFILING

R. G. Strauch
A. S. Frisch
R. A. Kropfli
B. L. Weber

Wave Propagation Laboratory
Boulder, Colorado
December 1985

UNITED STATES
DEPARTMENT OF COMMERCE

Malcolm Baldrige,
Secretary

NATIONAL OCEANIC AND
ATMOSPHERIC ADMINISTRATION

Anthony J. Calio,
Administrator

Environmental Research
Laboratories

Vernon E. Derr,
Director

BEST COPY AVAILABLE

NOTICE

Mention of a commercial company or product does not constitute an endorsement by NOAA Environmental Research Laboratories. Use for publicity or advertising purposes of information from this publication concerning proprietary products or the tests of such products is not authorized.

For official distribution--distribution authorized to U.S. Government Agencies and their contractors (specific Authority AR530-1) 23 October 1985.

BEST COPY AVAILABLE

CONTENTS

		Page
OVERVIEW		2
1.	WIND MEASUREMENTS WITH MICROWAVE RADARS	4
	1.1 Meteorological Radar Equation	4
	1.2 Radar Reflectivity for Water Particles	5
	1.3 Radar Reflectivity for Natural Aerosols	8
	1.4 Refractive Turbulence	8
	1.5 Signal Processing	12
	1.6 Wind Measurement Techniques	15
	1.7 References	17
2.	BOUNDARY LAYER PROFILING WITH X-BAND DOPPLER RADAR	20
	2.1 Introduction	20
	2.2 The Nature of CBL Echoes	20
	2.3 The VAD Method for Profiling Wind and Turbulence	22
	2.4 Case Study	26
	2.5 Summary and Conclusions	32
	2.6 References	33
3.	STATISTICAL ANALYSIS OF THE HEIGHT COVERAGE OF 50-, 405-, AND 915-MHz RADAR WIND PROFILERS	34
	3.1 Radar Sensitivity Comparisons	36
	3.2 Archiving	36
	3.3 Profiler Outages	37
	3.4 Distribution of Outages	39
	3.5 Height of Outages	41
	3.6 Summary and Conclusions	46
	3.7 References	46
APPENDIX - DOPPLER RADAR PROFILES		48

BEST COPY AVAILABLE

A FEASIBILITY STUDY ON THE USE OF FIREFINDER RADAR FOR WIND PROFILING

ABSTRACT

Firefinder, a microwave battlefield radar used for weapon location, can provide wind information for artillery control in some meteorological conditions. Theoretical considerations and experimental evidence indicates that Firefinder could produce wind measurements at low altitudes in the optically clear atmosphere, in precipitation, and in many clouds, but the radar wavelength is too short for routine wind measurements in the optically clear atmosphere above the boundary layer.

BEST COPY AVAILABLE

OVERVIEW

Objective

Various meteorological ("weather") research radars and MST (mesosphere-stratosphere-troposphere) research radars have shown that vertical profiles of atmospheric winds can be measured by Doppler radars. Therefore, because wind information is necessary for many military and civilian problems and because development of new radar systems devoted solely to wind measurements is costly, the question of using existing (operational) radars for "wind profiling" arises. This report examines the feasibility of using a microwave military radar, the Firefinder, for measuring battlefield wind conditions. The resulting wind data would be used to improve the accuracy of battlefield artillery. We wish to determine what wind information (even though not ideal or totally satisfactory) this existing battlefield radar can provide before undertaking the design and development of a new radar that could provide wind data ideally suited for gun placement.

An analogous situation exists with weather radars: The National Oceanic and Atmospheric Administration (NOAA) of the Department of Commerce, the Federal Aviation Administration of the Department of Transportation, and the Air Weather Service of the Department of Defense are collaborating on the development of a new weather radar system, NEXRAD (Next-Generation Weather Radar), that will replace the existing national weather radar network. The new NEXRAD radars will be 10-cm wavelength Doppler radars. At the same time, wind Profiler research work at NOAA has shown that radar wavelengths of about 0.7 to 7 m are most suitable for measuring winds in the troposphere. (A demonstration network of 30 of these wind Profilers is planned.) The NEXRAD radars will not be suitable for providing wind profiles under all conditions, but they will have very good wind profiling capability in precipitation and at low levels in the optically clear atmosphere. In addition they could possibly to be used in automated balloon tracking or automated cloud motion measurements to provide some wind data. From an economic viewpoint it would be desirable to have the NEXRAD radars provide wind profiles or to perform part of the functions of a wind Profiler rather than have completely new and separate radars for wind profiling.

BEST COPY AVAILABLE

NEXRAD and Firefinder radars have many similarities for wind measurements--both can measure winds in precipitation, both could be used to measure winds at cloud heights, both could be used to measure winds by tracking balloons or chaff, but both operate at a wavelength that is too short for routine measurement of winds to 8-10 km MSL in the optically clear atmosphere. Nonetheless, it may be cost-effective to use the limited wind profiling capabilities of these radars.

This report examines the problems of using microwave radars for wind profiling. The experiences of NOAA's Wave Propagation Laboratory (WPL) with 3-cm radars are also summarized, and the results of a 3-cm radar experiment are analyzed. In addition, the results of 2 years of operation of radar wind Profilers with 0.33-, 0.74- and 6.0-m wavelengths and an FM-CW radar with 0.1-m wavelength are examined to predict what performance might be expected with Firefinder and to judge what radar wavelength would be needed for reliable operation to a particular altitude.

Conclusions

On the basis of experimental and theoretical considerations, the Firefinder radar could produce (with proper data processing) horizontal wind measurements in precipitation, in the planetary boundary layer in optically clear air, intermittently at heights above the boundary layer in clear air, at cloud height for most types of clouds, and in special situations where weak-flying insects or large seeds are available as wind tracers. However, Firefinder, because of its short wavelength, cannot be relied on to provide routine wind observations above the boundary layer in the optically clear atmosphere. The altitude coverage in the optically clear air will vary widely depending on location, season of the year, and time of day. In summer convection, wind data could extend to several kilometers above ground while in winter or at night height coverage will often be limited to below 1 km. Therefore the decision of whether to use Firefinder for wind profiling depends on the cost required to modify the radars' data system for wind measurements and whether the limited wind data that would be provided would be valuable for artillery control or other battlefield problems such as visibility prediction.

BEST COPY AVAILABLE

1. WIND MEASUREMENTS WITH MICROWAVE RADARS

Most of the wind measurements that have been made with microwave radars involve scattering from hydrometeors. Radar reflectivity of rain, snow, or clouds with large particles (particle diameter of 100 μm or larger) is sufficient to obtain signal-to-noise ratios (SNR) that are high enough to measure mean radial velocities accurate to 1 m/s or better using radars with modest sensitivity. Since about 1970, radars have routinely provided wind data in meteorological research programs; Preprint Volumes of the Conferences on Radar Meteorology dating from about then summarize the progress. With the advent of digital data processing technology the meteorological Doppler radar became ready for transfer from research to operational use. The NEXRAD radar development is primarily the result of meteorological research and advances in data processing technology; the basic radar technology has been available since the development of the first weather radars nearly 30 years ago. Wind measurements in the optically clear atmosphere have also become routine in the past 10 years with research radars. However, most of this research has been performed with longer wavelength radars. Relatively little has been done with microwave radars because they are limited in the altitudes they can observe. The only microwave radar developed specifically for observations in the optically clear atmosphere is the high-resolution 10-cm-wavelength FM-CW radar first developed by Richter (1969); later a similar radar with Doppler capability was developed (Strauch, 1976). These radars are primarily high-resolution boundary layer research tools. Microwave radars have been used to determine the origins of clear-air returns (Hardy and Katz, 1969) but have not been used to measure routinely clear-air signals, as have longer wavelength radars.

1.1 Meteorological Radar Equation

The radar equation commonly used in meteorology is given by Probert-Jones (1962) as

$$\overline{P_r} = \frac{c}{1024 \cdot^2 \ln 2} [P_t \tau \lambda^2 G_o^2 \theta \phi] \eta / R^2 \qquad (1.1)$$

BEST COPY AVAILABLE

where

$\overline{P_r}$ is the received power, averaged over many independent realizations of the position of the scatterers (W)

c is the velocity of propagation (m/s)

P_t is the transmitted power (W)

τ is the pulse duration (s)

λ is the radar wavelength (m)

G_o is the on-axis gain of the antenna (Gaussian beam pattern assumed)

θ, ϕ are the half-power beamwidths of the antenna

η is the radar reflectivity (m^{-1}) or radar cross section per unit volume

R is the range to the radar resolution cell, i.e., the volume defined by the angular resolution of the antenna and the radial resolution of the radar pulse.

The following parameters are chosen to illustrate the signal levels with a radar of modest sensitivity:

λ = 10 cm

P_t = 100 kW

τ = 1 μs

G_o = 36 dB

$\theta = \phi$ = 0.05 radians.

The antenna diameter is about 2.5 m. The receiver noise level is assumed to be -110 dBm, and for this radar the signal power will exceed noise power at a range of 10 km for $\eta > 5.8 \times 10^{-13}$ m^{-1}.

1.2 Radar Reflectivity for Water Particles

The radar reflectivity for small-spherical raindrops is given by

$$\eta = \frac{\pi^5}{\lambda^4} |K|^2 Z \qquad (1.2)$$

BEST COPY AVAILABLE

where $K = (m^2-1)/(m^2+2)$ and m is the complex refractive index of the water spheres. Z is the "radar reflectivity factor," the average value of the sum of the sixth power of the diameters of the spherical drops per unit volume: $Z = (\Sigma D^6)/V$ where V is the volume of the radar resolution cell and the summation is for all particles in V. Z is commonly expressed in mm^6/m^3 or in decibels relative to 1 mm^6/m^3 (dBZ).

At 10-cm wavelength, $|K|^2 = 0.93$, so that for the illustrative radar parameters, Z must be greater than about 0.2 mm^6/m^3 or Z > -7 dBZ to obtain a signal that exceeds receiver noise at 10-km range.

The reflectivity factors for typical rainfall rates are summarized by Atlas (1964). The relationship developed by Marshall and Palmer (1948) is commonly used:

$$Z(mm^6/m^3) = 200\ R_a^{1.6} \qquad (1.3)$$

where R_a is the rainfall rate in millimeters per hour. Reflectivity factor values from this relationship are given in Table 1.1. Our illustrative radar would receive a signal equal to receiver noise from very light precipitation at a range of 10 km.

Table 1.1--Reflectivity factor values from the relationship of Marshall and Palmer (1948)

	R_a (mm/h)	Z (mm^6/m^3)	dBZ
Mist	0.05	1.6	+2
Drizzle	0.25	21.7	+13.4
Light rain	1	200	+23
Moderate rain	4	1.8 × 103	+32.5
Heavy rain	16	1.7 × 104	+42.3

Radar reflectivity factors for clouds and fog can be related to the total liquid water content (Atlas, 1964) by

$$Z = 0.048\ M^2 \qquad (1.4)$$

where M is the liquid water in grams per cubic meter. Typical liquid water content ranges from 0.05 to 0.2 g/m^3 in fog and 0.05 to 3 g/m^3 in clouds

BEST COPY AVAILABLE

Table 1.2--Liquid water content of fog and clouds

	M (g/m^3)	Z (mm^1/m^3)	dBZ
Fog	0.05 → 0.2	1.2×10^{-4} → 2×10^{-3}	-40 → -27
Clouds	0.05 → 3	1.2 × 10-4 → 0.4	-40 → -4

(Mason, 1971); see Table 1.2. Since the reflectivity of single spherical drops is proportional to the sixth power of the drop diameter, it is obvious that drop size distribution is very important in determining whether a radar will detect a given cloud. If the water drops are all of the same diameter, then the radar reflectivity factor is $Z = ND^6$ where N is the density of drops (m^{-3}). In terms of liquid water

$$Z = \frac{6 \times 10^3}{\pi} MD^3 \qquad (1.5)$$

for drop size in millimeters and M in grams per cubic meter.

Figure 1.1 shows the relationship between the radar reflectivity factor and liquid water for various drop sizes. It is apparent that our illustrative

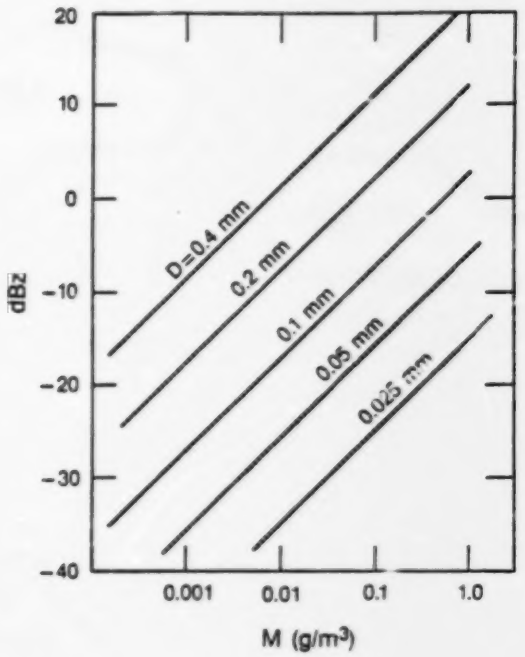

Figure 1.1.--Radar reflectivity factor dBZ as a function of lfiquid water content M for monodispersed water droplets of diameter D.

BEST COPY AVAILABLE

10-cm-wavelength radar would return a signal equal to receiver noise only for clouds containing precipitation-sized particles.

1.3 Radar Reflectivity for Natural Aerosols

The reflectivity factor for naturally-occurring atmospheric aerosols can be computed for typical aerosol distributions. The size distribution and number density of aerosol particles vary widely in time and space. Using observations by Junge (1964) on particle size distributions and the results of a general survey by Bullrich (1964), Mitchell (1966) showed that the reflectivity factor for natural aerosols could be expressed as

$$Z = 1.16 \times 10^{-2} D_{max}^3 \ (mm^6/m^3)$$

where D_{max} is the largest diameter particles for which the Junge distribution is applicable. Most measured values of aerosol distributions (Blifford, 1971) indicate that the Junge distribution should be valid to at least 0.01-mm-diameter particles, giving a contribution to the reflectivity factor of about 10^{-8} mm^6/m^3. A single particle of diameter 0.05 mm (per cubic meter) would have a reflectivity factor of 1.5×10^{-8} mm^6/m^3, so the radar reflectivity of aerosols is determined by the few large particles rather than the background distribution of small particles. The reflectivity factor for aerosols will be much less than that of small-particle clouds, so unless the radar sensitivity allows detection at about -60 dBZ, typical atmospheric aerosols can be ignored as a wind tracer for microwave radar. However, microwave radars will detect large particles, such as seeds, that occur at particular locations and during some seasons, and these particles can be used as wind tracers.

1.4 Refractive Turbulence

The recent interest in "wind profiling" with radars began with observations that VHF radars (6-10 m wavelength) could detect scattering routinely from the optically-clear atmosphere. The VHF work has been summarized by Gage and Balsley (1978). Although the theory for scattering from refractive index perturbations was developed on the basis of work with shorter wavelengths (Hardy and Katz, 1969), the shorter wavelength radars did not observe scattering throughout the troposphere; therefore, the idea of

BEST COPY AVAILABLE

using radar to measure winds operationally was not practical until VHF radars were developed for atmospheric probing. At this time there are wind profiling radars operating at VHF and UHF in a network in Colorado (Strauch et al., 1984).

Radar signals from the optically clear atmosphere are the result of perturbations in refractive index in the propagation path of the radar waves. These perturbations are caused by changes in temperature or humidity and can be described by their spatial spectrum. The radar backscattered signal intensity is proportional to the amplitude of the spatial spectral component of refractivity at scale size $\lambda/2$. Alternately, the refractive index field can be described by the structure function,

$$D_n(\vec{r}) = \overline{[n(x) - n(x + \vec{r})]^2} \qquad (1.6)$$

where n is the refractive index and r is a separation variable. For homogeneous and isotropic turbulence, Tatarski (1961) shows that the structure function can be expressed as $D_n(r) = C_n^2 \, r^{2/3}$ for separations between the "inner scale" l_o and "outer scale" L_o, where C_n^2 is the refractive index structure constant. Whenever the scale size $\lambda/2$ lies between l_o and L_o, the inertial subrange of turbulence, the radar reflectivity is given by Ottersten (1969) as

$$\eta = 0.38 \, C_n^2 \, \lambda^{-1/3} \, . \qquad (1.7)$$

If the inner scale is larger than $\lambda/2$, then radar reflectivity decreases because the turbulent fluctuations of n are damped by viscosity. The inner scale increases with altitude, so the failure of shorter wavelength radars to detect clear-air scattering at mid- and upper-tropospheric heights is generally believed to be caused by viscous cutoff of the half-wavelength scales of refractive turbulence. The spectrum of refractive turbulence for scale sizes less than l_o has been studied by Hill (1978). A critical wavelength for clear-air radars can be calculated from the kinematic viscosity and the level of mechanical turbulence; Fig. 1.2 shows this cutoff wavelength as a function of altitude and eddy dissipation rate (ε). This figure shows why 10-cm and shorter wavelength radars cannot routinely observe radar scattering above the boundary layer. These radars detect elevated scattering

BEST COPY AVAILABLE

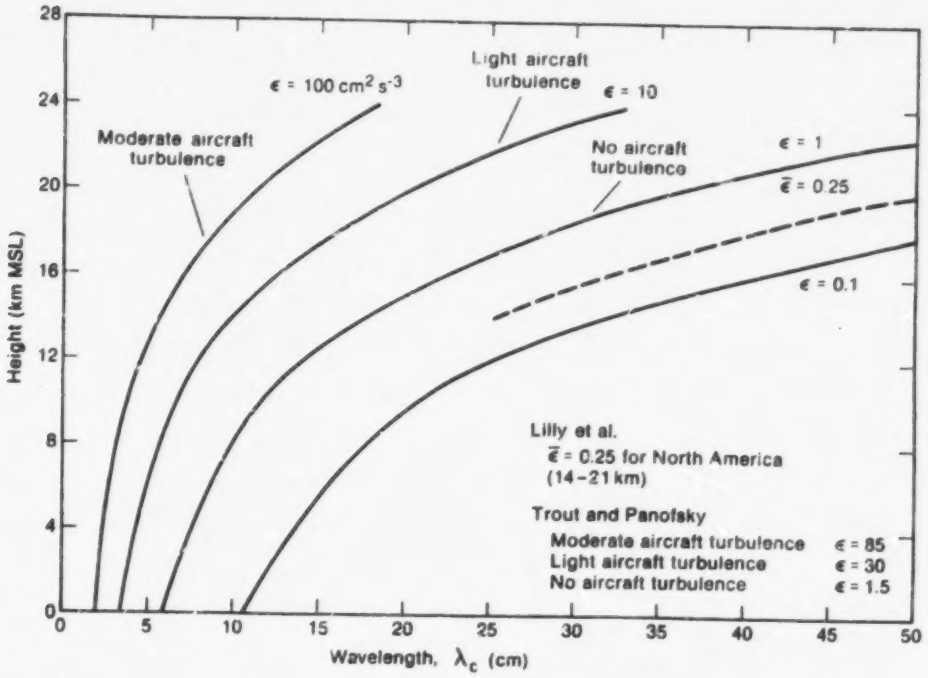
Height (km MSL)
Wavelength, λ_c (cm)
ϵ = 100 cm^2 s^{-3}
Moderate aircraft turbulence
Light aircraft turbulence
ϵ = 10
No aircraft turbulence
ϵ = 1
$\bar{\epsilon}$ = 0.25
ϵ = 0.1
Lilly et al.
$\bar{\epsilon}$ = 0.25 for North America (14–21 km)
Trout and Panofsky
Moderate aircraft turbulence ϵ = 85
Light aircraft turbulence ϵ = 30
No aircraft turbulence ϵ = 1.5

Figure 1.2.--Radar cutoff wavelength λ_c vs. height for various levels of eddy dissipation ε. Clear air radar wind profiling should be possible if the radar wavelength exceeds λ_c. Eddy dissipation rates (mechanical turbulence) measured by aircraft (Lilly et al., 1974; Trout and Panofsky, 1969) are listed.

layers when mechanical turbulence is sufficiently high, but they cannot detect scattering from the normal background of refractive turbulence. However, longer wavelength radars of comparable sensitivity do detect scattering at all heights in the troposphere. The steep slopes of the curves in Fig. 1.2 suggest a dramatic improvement in height coverage for a clear-air radar as the wavelength increases from 10 to 40 cm. This is observed in the Colorado Profiler network where a 0.33-m radar measures wind profiles to 8 km MSL routinely and often to 12-14 km MSL whereas more sensitive 10-cm radars are unable to do so. This empirical observation is the major reason that operational radars such as NEXRAD or Firefinder are not proposed for wind profiling.

Measurements of boundary layer C_n^2 with a 10-cm radar (Chadwick et al., 1978) show typical values of 10^{-15} $m^{-2/3}$. Figures 1.3 and 1.4 show hourly and monthly cumulative probability distributions of C_n^2 at 805 m above ground in Colorado. For C_n^2 of 10^{-15} $m^{-2/3}$, the radar reflectivity for a 10-cm radar is

BEST COPY AVAILABLE

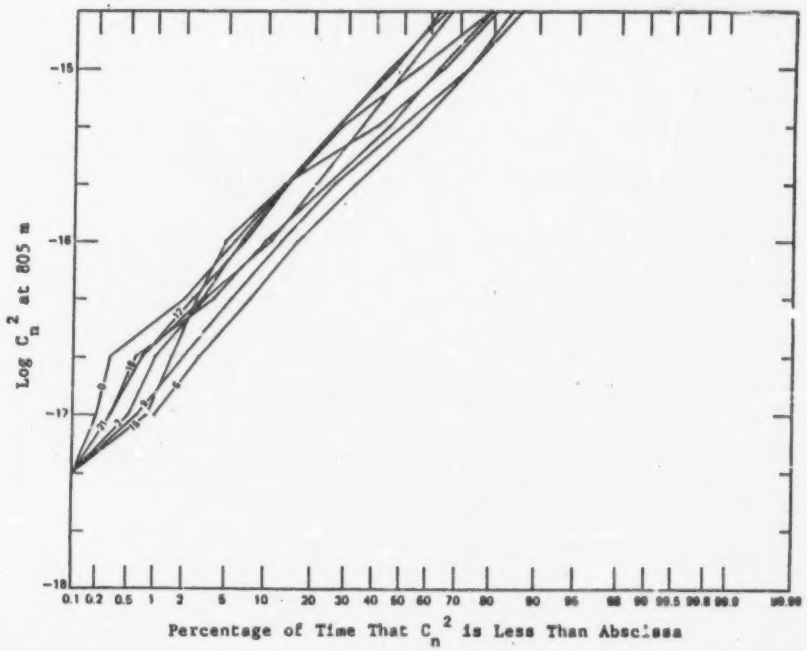

Figure 1.3.--Probability distribution of certain hourly log C_n^2 values.

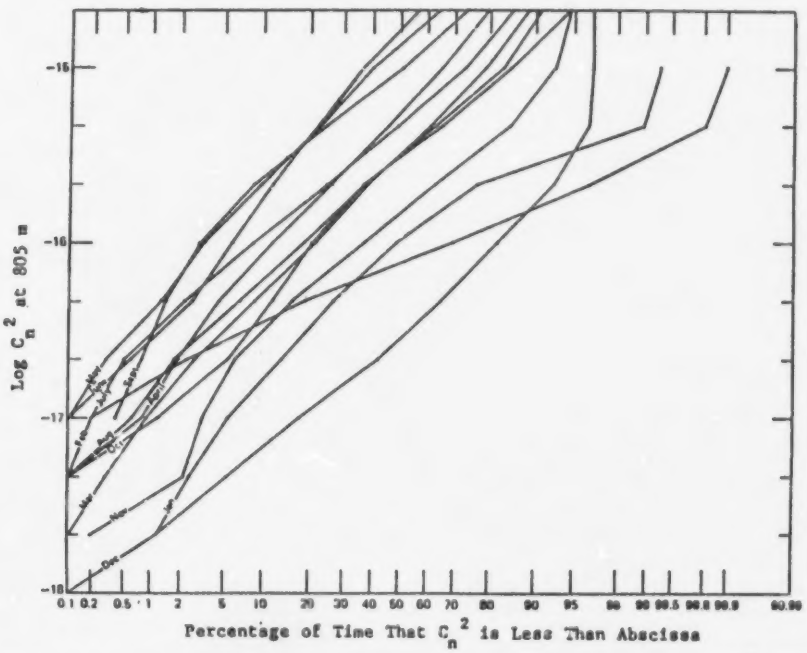

Figure 1.4.--Probability distribution of monthly log C_n^2 values.

BEST COPY AVAILABLE

1.7×10^{-15} m^{-1}; about 25 dB below the reflectivity needed to yield a signal equal to noise at 10-km range, with out illustrative radar.

Although 10-cm radars do not usually observe scattering from the optically clear air above the boundary layer, scattering is sometimes observed in layers where mechanical turbulence is enhanced or in the vicinity of clouds (particularly cloud tops) where evaporation enhances temperature and moisture fluctuations. Thus, clouds can sometimes be detected by 10-cm-wavelength radar even though scattering by the particles is too weak to detect. When clouds are detected by 10-cm radar, it is not always possible to determine whether the scattering is by small particles or refractive turbulence. In either case, the Doppler radar can use the signal as a tracer for mean wind because the fall speed of the small particles can be neglected.

1.5 Signal Processing

It is apparent that the radar parameters used to illustrate the signal levels do not yield detectable signals using Eq. (1.1), except in precipitation. Equation (1.1), however, applies to the output of the receiver and does not account for SNR improvements by signal processing and averaging. An SNR at the receiver output has been used only to illustrate the signal levels obtained from various scattering mechanisms. However, because clear-air radars take advantage of averaging, the sensitivity is not determined by signal-to-mean noise power at the receiver output but rather signal-to-rms noise fluctuations at the averaged output. Therefore, clear-air radars can detect (and measure velocity) when input SNR is much less than 1. Doppler radar processing combines coherent integration (SNR improvement proportional to observation time) and incoherent integration (detection improvement proportional to the square root of observation time). Coherent integration time is limited to the coherence time of the signals. If all available coherent integration time is used (as is typically the case for clear-air radars), the minimum detectable reflectivity for total observation time T_o is given by (Strauch, 1976)

BEST COPY AVAILABLE

$$\eta_{min} = \frac{128\, R^2\, k\, T_{op}\, W\, L_F\, L_T\, L_R}{\overline{P_t}\, A_e\, \Delta R \sqrt{\pi \lambda \Delta V T_o}} \qquad (1.8)$$

where

R is the range to the scattering volume (m)

k is the Boltzman constant

T_{op} is the system noise temperature given by

$$T_{op} = \frac{T_{ANT}}{L_R} + (1 - 1/L_R)T_{LR} + T_R$$

T_{ANT} is the antenna temperature (K) (at the antenna port)

L_R is the RF loss in the receiver path (from the antenna port to the receiver)

T_{LR} is the temperature of the loss in the receiver path (K)

T_R is the receiver noise temperature (K)

W is the width of the Doppler spectrum (m/s)

L_F is the loss in the receiver filter

L_T is the RF loss in the transmitter path (from the transmitter to the antenna port)

$\overline{P_t}$ is the average transmitted power (W)

A_e is the effective aperture of the antenna (m^2)

ΔR is the range resolution (m)

λ is the radar wavelength (m)

ΔV is the velocity resolution of the Doppler analyzer (m/s)

T_o is the total observation time (s).

Equation (1.8) results from (1.1) and the following:

(a) two general antenna relationships,

$$G_o = \frac{4\pi A_e}{\lambda^2} \quad \text{and} \quad G_o \theta\phi \doteq \pi^2$$

(b) accounting for system losses ($L_F\, L_R\, L_T$)

(c) expressing receiver noise in terms of system noise temperature

(d) expressing transmitted power in terms of average value

BEST COPY AVAILABLE

(e) improving SNR by coherent integration, $\lambda/2T\sqrt{2\pi}\ W$ (Strauch, 1976)

(f) reducing noise fluctuations from incoherent processing, $2T_o \Delta V/\lambda$ (Strauch, 1976)

(g) equating signal-to-rms noise fluctuations to unity to define the minimum detectable signal.

For our illustrative radar,

Top ~ 600 K for a receiver noise level of -110 dBm and a receiver bandwidth matched to a 1-μs pulse

Ae ~ 3.2 m^2 for a 36-dB gain antenna

ΔR ~ 150 m for a 1-μs pulse.

Other typical values are:

W = 1 m/s for the spectrum width

$\overline{P_t}$ = 500 W (1-μs pulse width and 2000 pulses/s)

ΔV = 0.25 m/s

L_p = 1.7 or 2.3-dB loss for a matched filter (Doviak and Zrnic, 1978)

L_T = 1.25 (1-dB loss in transmitter path; this is the loss following the point where the transmitted power is measured to the antenna port)

L_R = 1.25 (1-dB loss from the antenna port to the receiver).

With proper signal processing the illustrative radar has a minimum detectable reflectivity at 10-km range of $\eta_{min} \doteq 4 \times 10\text{-}16\ m^{-1}$. This radar could detect scattering from hydrometeors at 10-km range when Z is greater than about $10^{-4}\ mm^6/m^3$, or -40 dBZ. It could detect scattering from refractive turbulence at 10 km if $C_n^2 > 5 \times 10^{-16}\ m^{-2/3}$. Therefore, this radar should detect most clouds, all types of precipitation, and scattering from the optically clear air in the boundary layer. If operated at high elevation angles and <u>if</u> the scattering intensity decreased with altitude as it does when observed with longer wavelength radars, the radar would have sufficient <u>sensitivity</u> to detect clear-air scattering well above the boundary layer. However, experience with sensitive 10-cm radars shows that the reflectivity decrease with altitude is much greater than it is for longer wavelengths, so microwave radars are limited in altitude coverage, and our illustrative 10-cm radar should have altitude coverage similar to that of 10-cm FM-CW radars.

BEST COPY AVAILABLE

1.6 Wind Measurement Techniques

The methods used to measure winds with radars depend on the type of antenna scanning available, the dwell time or observation time needed to obtain sufficient SNR for an accurate velocity measurement, and the assumptions that can be made about the wind field. VHF radars have limited scanning; typically only two to five antenna pointing positions are available. These radars use relatively long dwell times (0.5 to 5 min at each pointing position) to obtain the necessary SNR. Therefore a simple flow field is assumed, and profiles of mean winds are measured with relatively long averaging times. The elevation angles used by VHF radars are usually 60° or more above the horizon because VHF antennas for wind measurements are phased arrays with their mechanical axis pointed toward zenith. Microwave radars, by contrast, usually have steerable antennas and shorter observation times that allow rapid scanning when SNR is high. In these cases a more complex wind field can be described by the radar measurements. Most microwave radars are not designed to use long observation times with stationary or very slowly scanning antennas. The Firefinder or NEXRAD radars must be able to operate with both long and short dwell times if they are to be used for wind measurements.

The number of antenna pointing positions needed to measure the wind depends on the assumptions that are made about the wind field. Chadwick et al. (1984) analyze the problem in terms of an assumed linear flow field and two, three, five, or eight antenna pointing positions. The number of antenna pointing positions for microwave radars such as Firefinder allows a wide choice of scanning. Various scanning methods for single Doppler radars are described by Doviak and Zrnic (1984). Several of these methods are applicable to Firefinder when SNR is high (precipitation signals). The most often used microwave method is the VAD (velocity-azimuth display) analysis, which analyzes the wind field on the basis of radial velocities measured on a circle around the radar. This method is not suitable for Firefinder, but analysis on an arc, on a conical surface, or in a volume all could be used. When SNR is low (as in clear-air observations), then the number of pointing angles must be reduced so the observation time at each position can be increased. The simple two and three beam pointing positions used at VHF are also applicable with Firefinder because of the need to restrict the total observation time to

BEST COPY AVAILABLE

reduce the probability of detection of the radar location by countermeasure receivers.

The simplest scan is illustrated in Fig. 1.5; the antenna elevation angle is θ_E, and two pointing directions are used. The beam pointing directions are symmetrically displaced from the direction where the winds need to be measured (along the projectile trajectory). In the clear air or at low elevation angles, the vertical velocity can be ignored so that cross wind (u) and the wind along the projectile trajectory (v) are given by

$$u = \frac{V_1 - V_2}{2 \cos \theta_E \sin\phi} \quad \text{and} \quad v = \frac{V_1 + V_2}{2 \cos \theta_E \cos\phi}$$

where V_1 and V_2 are the measured radial velocities.

The standard deviations of the estimates of the components are

$$\sigma_u = \frac{\sigma_V}{\sqrt{2} \cos\theta_E \sin\phi} \quad \text{and} \quad \sigma_u = \frac{\sigma_V}{\sqrt{2} \cos\theta_E \cos\phi}$$

where σ_V is the standard deviation of the estimate of radial velocity.

For precipitation, let $\theta_E = 11.5$; the error due to fall velocity of the particles will be less than 1 m/s in most cases. The SNR will be high, so the radar should be able to measure winds to 5-km altitude (25-km range) with short observation time (< 5 s). Cross wind and wind along the track will have equal error for $\phi = 45°$: $\sigma_u = \sigma_v \doteq \sigma_V$.

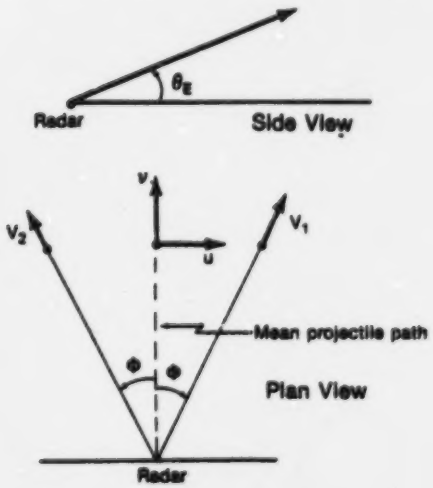

Figure 1.5.--Simple scan strategy for wind measurements with a 2-point scan. $\theta_E = 11.5°$ in precipitation and 30° in clear air.

BEST COPY AVAILABLE

In precipitation, σ_v will be 0.1 to 1 m/s, so ϕ could be reduced to put the measurement volumes closer to the trajectory. For $\phi = 20°$, the cross-wind error doubles but would still be about 1 m/s at most.

For clear air, the elevation angle could be increased to 30° to reduce the range to a given altitude. This increases σ_u and σ_v by about 1.13; however, the range is reduced to 10 km for a maximum altitude of 5 km. In clear air, σ_v will be about 1 m/s (to altitudes where scattering is detectable), so errors in u and v will be 1 to 2 m/s.

This simple scan strategy minimizes the time required to obtain a wind measurement, and the measurement volumes are near the projectile trajectory. Horizontally uniform flow must be assumed; u and v are assumed to vary only with altitude.

1.7 References

Atlas, D., 1964. Advances in radar meteorology. Adv. Geophys., 10, 317-378.

Blifford, I., 1971. Global aerosol models. NCAR Tech. Note NCAR-TN/PROC 68, National Center for Atmospheric Research, Boulder, CO.

Bullrich, K., 1964. Scattered radiation in the atmosphere and the natural aerosol. Advan. Geophys., 10, 99-260.

Chadwick, R.B., K.P. Moran, G.E. Morrison, and W.C. Campbell, 1978. Measurements showing the feasibility for radar detection of hazardous wind shear at airports. AFGL-TR-78-0160, Air Force Geophysical Laboratory, Hanscom AFB, MA.

Chadwick, R.B., A.S. Frisch, and R.G. Strauch, 1984. A feasibility study on the use of wind Profilers to support space shuttle launches. NASA Contractor Rep. 3861, National Aeronautics and Space Administration, Marshall Space Flight Center, AL.

Doviak, R.J., and D.S. Zrnic, 1978. The weather radar equation-receiver band width considerations. Preprints, 18th Conf. on Radar Meteorology, American Meteorological Society, Boston, MA, 484-489.

BEST COPY AVAILABLE

Doviak, R.J., and D.S. Zrnic, 1984. Doppler Radar and Weather Observations. Academic Press, New York, 458 pp.

Gage, K.S., and B.B. Balsley, 1978. Doppler radar probing of the clear atmosphere. Bull. Am. Meteorol. Soc., 59, 1074-1093.

Hardy, K.R., and I. Katz, 1969. Probing the clear atmosphere with high power, high resolution radars. Proc. IEEE, 57, 468-480.

Hill, R.J., 1978. Spectra of fluctuations in refractivity, temperature, humidity, and the temperature-humidity cospectrum in the inertial and dissipative ranges. Radio Sci., 13, 953-961.

Junge, C., 1964. Air Chemistry and Radio Activity. Academic Press, New York, 382 pp.

Lilly, D.K., D.E. Waco, and S.I. Adelfang, 1974. Stratospheric mixing estimated from high-altitude turbulence measurements. J. Appl. Meteorol., 13, 488-493.

Marshall, J.S., and W.M.K. Palmer, 1948. The distribution of raindrops with size. J. Meteorol., 5, 165-166.

Mason, B.J., 1971. The Physics of Clouds. Oxford Univ. Press, London and New York, 671 pp.

Mitchell, R., 1966. Radar meteorology at millimeter wavelengths. Air Force Rep. S3D-TR-66-117., Hanscom AFB, MA.

Ottersten, H., 1969. Atmospheric structure and radar backscattering in clear air. Radio Sci., 4, 1179-1193.

Probert-Jones, J.R., 1962. The radar equation in meteorology. Quart. J. Roy. Meteorol. Soc., 88, 485-495.

Richter, J.H., 1969. High resolution radar sounding. Radio Sci., 4, 1261-1268.

Strauch, R.G., 1976. Theory and application of the FM-CW Doppler radar. Ph.D. Thesis, Univ. of Colorado, Boulder.

BEST COPY AVAILABLE

Strauch, R.G., D.A. Merritt, K.P. Moran, K.B. Earnshaw, and D.W. van de Kamp, 1984. The Colorado wind profiling network. J. Atmos. Oceanic Technol., 1, 37-49.

Tatarski, V.I., 1961. Wave Propagation in Turbulent Medium. Translated by R.A. Silverman, McGraw-Hill, New York, 285 pp.

Trout, D., and H.A. Panofsky, 1969. Energy dissipation near the tropopause. Tellus, 21, 355-358.

BEST COPY AVAILABLE

2. BOUNDARY LAYER PROFILING WITH X-BAND DOPPLER RADAR

2.1 Introduction

In this section we examine the ability of 3-cm-wavelength radar to provide wind and turbulence profiles within the optically clear convective boundary layer (CBL). The discussion focuses on observations with two NOAA/WPL X-band Doppler radars during Phoenix II. The radar-derived profiles presented in the case study overlap with wind data taken on the 300-m-tall Boulder Atmospheric Observatory (BAO) tower located about 7 km from each radar.

2.2 The Nature of CBL Echoes

Although no exhaustive climatological study of CBL X-band radar echoes has been performed (as has been done with the S-band FM-CW radar; see Sec. 1.4) we have found that the WPL X-band radars generally observe sufficiently strong echo within the CBL to allow good Doppler velocity estimates to be made to distances of 15 km. Similar results have been obtained with a shorter wavelength K-band radar.

Echoes in the CBL have been observed with these radars from May through September during the daytime hours when the surface heat flux is strong ($\overline{w'T'} > 0.1$°C m/s) and the boundary layer is characterized by large vertical mixing. Low-level clear-air echoes during the winter months usually diminish to the point where velocity measurements are not reliable.

The 3-cm-wavelength radars considered here are not usually thought of as "clear air" radars because they are not sensitive to the refractive index fluctuations discussed in Sec. 1. In that section an average (S-band) reflectivity value of 1.7×10^{-15} m^{-1} was given for the 805-m level in northeast Colorado. Values about 20 dB stronger than this were observed by Kropfli et al. (1968) in the humid (but cloud free) boundary layer at Wallops Island, VA. Even these large values are about 20 dB too weak to account for the X-band reflectivities observed within the CBL in Colorado. In addition, the spatial distribution of these echoes, usually fairly uniform with height, is inconsistent with scatter from refractive index fluctuations, which results in

BEST COPY AVAILABLE

a well-defined reflectivity maximum near the top of the CBL. Therefore, the scattering mechanism responsible for the echoes described in this section is most likely particulate scatter from the small millimeter-sized particle lifted by buoyant parcels rising from the heated surface.

The sensitivity of these radars to particulates results from the radar cross section for particulate scatterers varying as λ^{-4}, as in Eq. (1.2). For example, a 3.2-cm-wavelength radar would have a 21-dB advantage over a 10.6-cm-wavelength radar from this wavelength dependency. We believe the scatterers sensed by these X-band radars are larger than aerosols, typically in the millimeter size range, and are probably insects, seeds, and other small particles. Recent observations made with NOAA X-band radar indicated a reflectivity or radar cross section per unit volume of 10^{-10} m^{-1}, which is in reasonable agreement with X-band targets identified by Hardy and Katz (1969) as being insects and having a reflectivity of 3×10^{-10} m^{-1}.

Evidence obtained so far indicates that the scatterers observed most often in Colorado do not have characteristics of "strong fliers." If they did, they could not be used as accurate tracers of air motion. We have not observed strong azimuthal dependence in the reflectivity field, as observed by Schaefer (1976) for swarms of migrating insects. His observations showed two strong reflectivity maxima at azimuths 180 apart, presumably the directions at which the insects were viewed from the side. In addition, the depolarized signal, which is also sensitive to the shape of the scatterers, has been examined with no azimuthal dependence being found (Pasqualucci et al., 1983). More convincingly, the comparisons of tower and radar measurements of horizontal velocity (given in Sec. 2.4) and other data sets show that there is no significant bias between the measurements.

To summarize the above, these echoes are often found to be strong and uniformly distributed throughout the CBL during the months from May through September in Colorado and they are usually not found during the winter months because of the weaker surface heating and absence of available particulates. The following sections will show how they have been used as tracers of the air motion.

BEST COPY AVAILABLE

2.3 The VAD Method for Profiling Wind and Turbulence[1]

If, instead of using a Doppler radar measurement along two directions as discussed in Sec. 1.6, we rotate the radar antenna 360 in azimuth at fixed elevation to measure the azimuthal variation of the Doppler velocity, $V_r(\beta)$, we can use the periodic azimuth variation of the radial velocity to measure wind profiles (Browning and Wexler, 1968). Figure 2.1 indicates the scan geometry.

If at particular height the local large-scale wind can be represented as a constant plus a linear variation in x (east) and y (north), the Doppler velocity is written as

$$V_r(\beta) = \frac{R}{2}\cos\theta\ \mathrm{DIV} + w_o \sin\theta + v_o \cos\theta \cos\beta + u_o \cos\theta \sin\beta - \frac{R}{2}\cos\theta\left(\left\langle\frac{\partial u}{\partial x}\right\rangle - \left\langle\frac{\partial v}{\partial y}\right\rangle\right)\cos 2\beta + \frac{R}{2}\cos\theta\left(\left\langle\frac{\partial u}{\partial y}\right\rangle + \left\langle\frac{\partial v}{\partial x}\right\rangle\right)\sin 2\beta \quad (2.1)$$

where R is the radius of the measurement circle as shown in the figure, θ is the elevation angle, β is the azimuth, and $\mathrm{DIV} = \langle \partial u/\partial x \rangle + \langle \partial v/\partial y \rangle$. Note that the more usual sign convention, i.e., V_r being positive for targets moving away from the radar, is used here in contrast to that found in Browning and Wexler (1968). The wind components u, v, and w with zero subscripts are the mean values over the measurement circle of radius R, and $\langle\ \rangle$ signifies an average over the circle.

A harmonic analysis of $V_r(\beta)$ can yield the following information about the mean kinematic properties of the wind:

(a) A weighted sum of divergence and vertical motion from the zeroth-order harmonic.

(b) The horizontal wind components, u_o, toward the east, and v_o, toward the north, from the first-order harmonics.

---

[1] A more complete discussion can be found in Probing the Atmospheric Boundary Layer, D. Lenschow, editor, to be published in 1986.

BEST COPY AVAILABLE

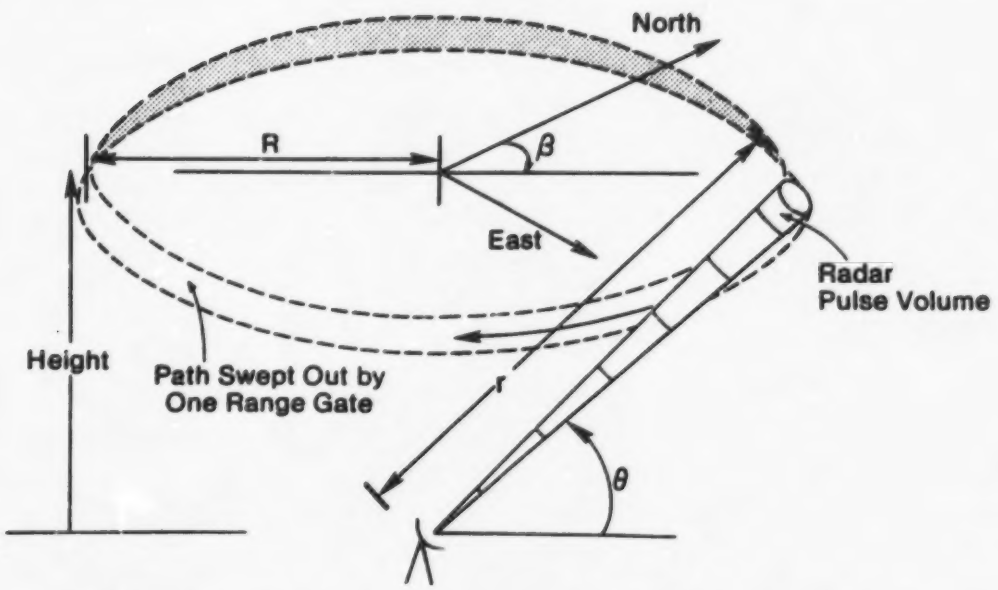

Figure 2.1.--Velocity-azimuth-display (VAD) scan geometry.

(c) Stretching deformation $\langle \partial u/\partial x \rangle - \langle \partial v/\partial y \rangle$ and shearing deformation $\langle \partial v/\partial x \rangle + \langle \partial u/\partial y \rangle$ from the second-order harmonics.

The usual procedure is to perform a least-squares fit of the data to an equation of the form

$$V_r(\beta) = A_o + A_1 \sin\beta + A_2 \cos\beta + A_3 \sin 2\beta + A_4 \cos 2\beta \ . \qquad (2.2)$$

The desired kinematic terms are found from the coefficients of this equation along with the known range and elevation angle.

In practice, when we examine a VAD, we observe a noisy sinusoidal variation of V_r with azimuth. The sinusoidal portion is the result of large-scale (relative to R) components of u, v, w, and DIV, and the superimposed noise-like signal is the result of small-scale turbulence and, to a lesser extent, random errors in the estimate of V_r.

A typical example of this is given in Fig. 2.2. These X-band radar data were taken in the CBL on 27 Sept. 1982, and they represent the data from one range gate at a height of 345 m during a scan at 45° elevation. Fitting a 360° sine wave by least squares, as shown in the figure, provides an excellent

BEST COPY AVAILABLE

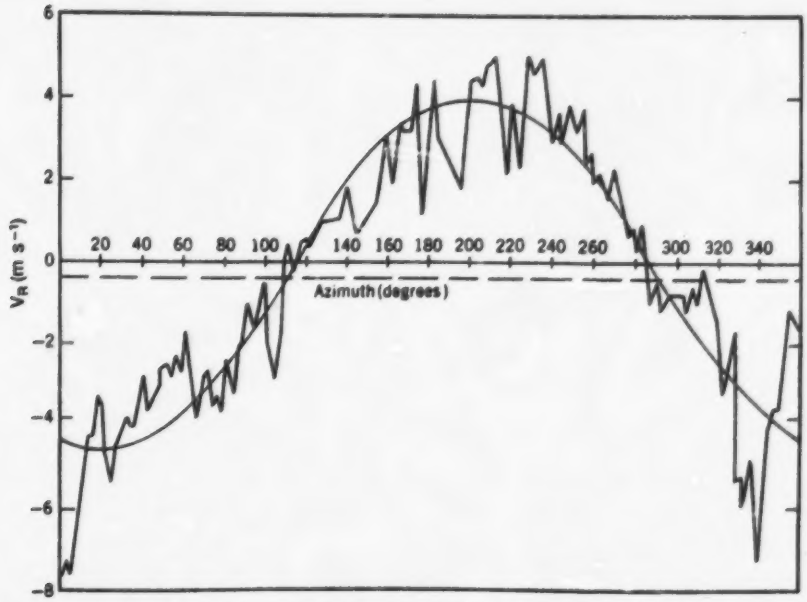

Figure 2.2.--A typical radial velocity vs. azimuth display, showing the effects of mean wind and small-scale turbulence at 345 m above the surface. The least-squares fit is indicated.

measure of the mean wind components, u_o and v_o, and the sum of the first two terms in Eq. (2.1), which we represent as $f(w_o,DIV)$. In this analysis we had set A_3 and A_4 in Eq. (2.2) to zero, since we were not interested in deformation here. The two terms constituting $f(w_o,DIV)$ can provide a measure of w_o when the elevation angle is high ($\cos^2\theta \ll 1$) and a measure of divergence at low elevation angles ($\sin\theta \ll 1$). An elevation of 45° is an intermediate case, and a separation of w and DIV cannot be made unless further assumptions are used.

As shown in the figure, there is a significant amount of scatter about the best-fit sine curve. The scatter here is not measurement noise but is actually the turbulent signal so important in many CBL studies. We have implemented an analysis method similar to that of Wilson (1970) in which these fluctuations are processed to yield profiles of second-order turbulence quantities such as $\overline{u'w'}$, $\overline{v'w'}$, $\overline{u'v'}$, $\overline{w'^2}$, and $\overline{u'^2} + \overline{v'^2}$ where (') represents turbulent scale fluctuations larger than the radar pulse (~50 m). A discussion of this method is not presented here, but results of such calculations are presented in the Appendix along with profiles of mean wind components.

BEST COPY AVAILABLE

The accuracy of the wind components derived from a full VAD analysis is good; the expected error is generally less than about 0.15 m/s. Expected errors for the wind components are computed from the "measurement matrix" of the least-squares-fit analysis (Mathews and Walker, 1965) and are found to be

$$\sigma_u = \sigma_v = \left[\frac{2VAR(V_r)}{N} \sec^2\theta\right]^{1/2} \tag{2.3a}$$

and

$$\sigma_w = \left[\frac{VAR(V_r)}{N} \csc^2\theta\right]^{1/2} \tag{2.3b}$$

where N is the number of samples used in the least-squares fit and $VAR(V_r)$ is the variance of the measurements about the best-squares fit. Figure 2.3 shows how these errors vary with elevation when N = 200 and $VAR(V_r) = 1\ m^2/s^2$. Scatter plots of u and $\overline{u'w'}$ shown in Figs. 2.4a and 2.4b were derived from data taken independently from the WPL K-band and X-band radars when they were co-located and performing identical scans. Each point in the figure represents an independent measurement by each radar at the same range gate. The small amount of scatter demonstrates the precision of the technique to measure wind and turbulence profiles.

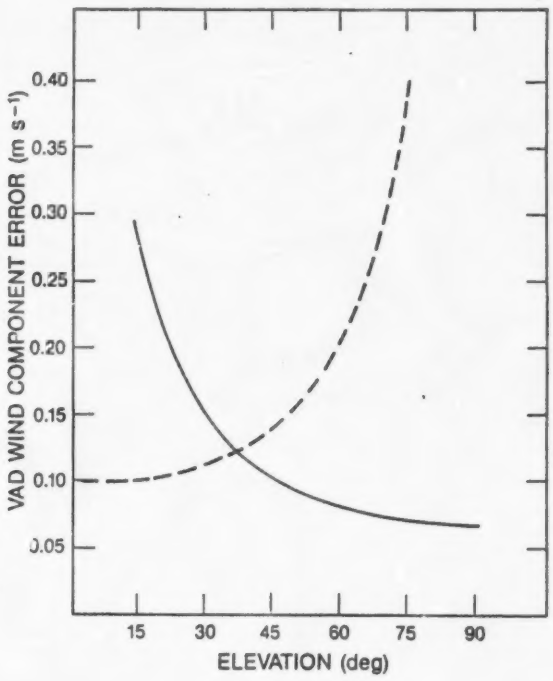

Figure 2.3.--Error estimates of the wind components derived from least-squares-fit analysis of VAD data. Two hundred rays of data and a standard deviation of 1 m/s about the best-fit curve were assumed. The dashed curve represents the error in a horizontal wind component and the solid curve is the error in w when DIV = 0.

BEST COPY AVAILABLE

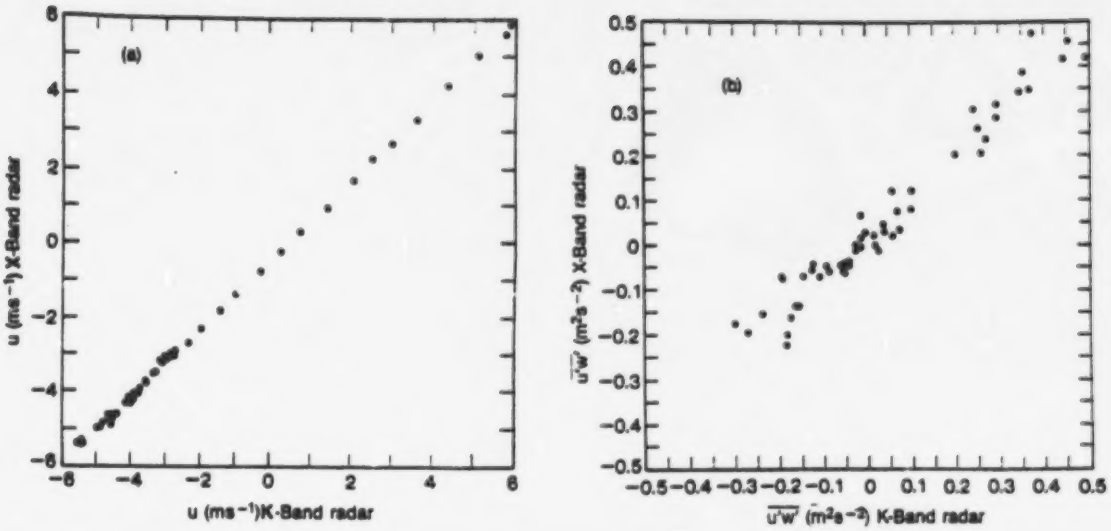

Figure 2.4.--Scatter plot of (a) u and (b) $\overline{u'w'}$ at corresponding range gates derived from colocated X-band and K-band radars scanning simultaneously in the VAD mode at 45° elevation on 14 February 1984.

2.4 Case Study

The Phoenix II planetary boundary experiment was an intensive effort sponsored jointly by the National Science Foundation (NSF), Army Research Office (ARO), and NOAA to document the evolution of the CBL with Doppler radar, instrumented aircraft, a surface network, and an instrumented tower. Figure 2.5 indicates the locations of the NOAA X-band radars, the BAO tower, and other instruments not considered in this analysis. The X-band radar parameters are summarized in Table 2.1.

Most of the radar data sets consisted of coordinated sector scans by two pairs of Doppler radars, each covering a 10 km × 10 km area with ~200-m resolution. In these studies chaff was used to enhance the echo strength within the boundary layer. However, on 28 June 1984, no chaff was released and naturally occurring particulates were used as air motion tracers. The Doppler radars were operated in the VAD mode from about 0900 to about 1600 MST to provide a continuous record of wind and turbulence profiles over each radar. A 2-h interval of this data from 1040 to 1240 MST was processed and analyzed, and a discussion of this analysis follows.

During the entire period, each of the X-band radars was programmed to scan through a series of six conical scans from 5° elevation through 80°

BEST COPY AVAILABLE

Table 2.1--Parameters of the NOAA/WPL X-band radars

Wavelength	3.22 cm
Peak power	50 kW
Pulse duration	0.75 μs
Average power	47 W
Pulse repetition period	800 μs
Antenna diameter	3.1 m
System gain	44 dB
Beamwidth	0.8
Noise power	-109 dBm
Minimum detectable reflectivity at 10 km	-18 dBZ

elevation in 15 steps. Each full revolution of the antenna was completed in 30 s so that each sequence was repeated every 3 min. The 180 beams of data acquired with each revolution had a dwell time of 0.17 s.

As explained in Sec. 2.3, this variety of elevation angles allows an accurate determination of all the turbulent variances and covariances as well as all three wind components. The lower elevations, <35°, provide the most

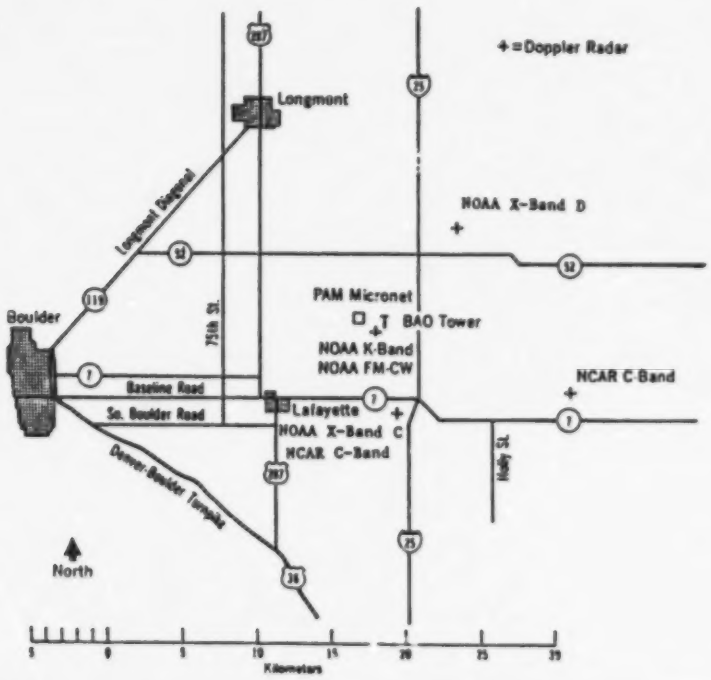

Figure 2.5.--Map showing the Phoenix II experimental layout.

BEST COPY AVAILABLE

accurate horizontal wind and turbulence information, and the highest elevation, 80°, provides the most accurate vertical wind component and turbulence information. Intermediate elevations, 50° and 65°, provide the most accurate estimates of the Reynolds stress quantities, $\overline{u'w'}$ and $\overline{v'w'}$, in which both horizontal and vertical wind fluctuations contribute.

Although most of this 2-h data set was processed, the scans at 35 and 80° are most illustrative of the utility of this method, and only these are included for discussion in this report. The 2-h data set was divided into three intervals of about 40 min each to facilitate comparison with mean wind quantities readily available from the BAO tower. Thus, in what follows we refer to Period I from 1040 to 1120, Period II from 1120 to 1200, and Period III from 1200 to 1240 MST. Data for these periods are plotted as time-height cross sections and as wind and turbulence profiles averaged for each period. The field plotted, elevation angle, radar, and time interval are indicated on each plot. During each period 12 to 14 scan sequences were performed at 3-min intervals. No smoothing or data filling was performed on the cross sections. Although a complete analysis of even this abbreviated sample is beyond the scope of this report, some relevant features will be discussed here.

Figures in the Appendix show that reliable velocity and covariance data are obtained for heights from about 0.25 km to well above 1.5 km at times. An overly conservative error criterion was used in the selection of data that were plotted in these figures so that uncertainty of the plotted results would be no greater than about 0.15 m/s. By relaxing this criterion somewhat, we could have plotted velocity estimates all the way to about 3 km with errors no greater than about 0.4 m/s. In general it would be expected that relaxing this error criterion would increase the maximum height of the profiles, though the amount of the increase would be impossible to predict without further study.

We now look in more detail at the scatterers that provided these echoes. Figure 2.6 shows the increase in the height of the capping inversion with time as determined from three balloon releases during the case study. The soundings indicate that the mixed layer never grew deeper than about 1.9 km during this time. Nevertheless, the plots in the Appendix indicate that echo was often observed well above this level, and, as just mentioned, the actual echo often exceeded the indicated echo top by a kilometer.

BEST COPY AVAILABLE

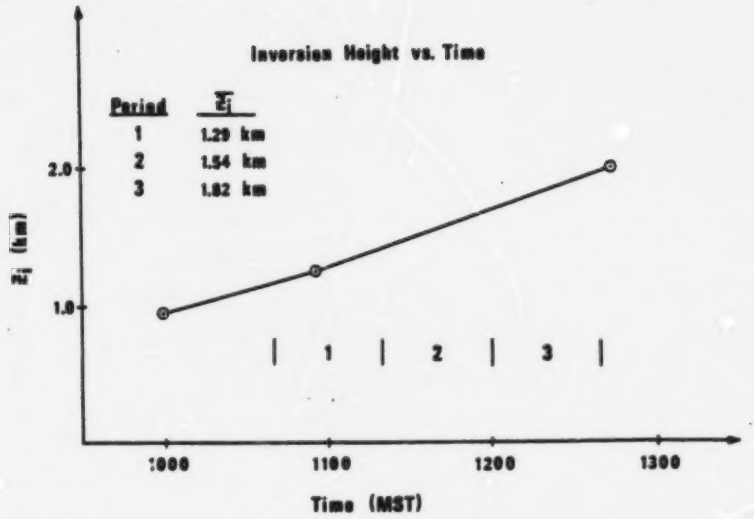

Figure 2.6.--Height of the capping inversion vs. time from three balloon releases near the BAO tower on 28 June 1984.

Some insight can be gained by considering the time-height cross section of the echo observed by the NOAA/WPL FM-CW radar (Fig. 2.7). (This radar was operated in a mode that does not provide velocity estimates during the time shown.) Since time increases from right to left, Fig. 2.7 shows a gradually deepening mixed layer consistent with the three soundings, but at the same time a layer of point targets descends from about 2.6 km to about 2.0 km. This descending layer is also apparent in the plots for NOAA X-band radar C but not for X-band radar D because of the rejection criterion mentioned above.

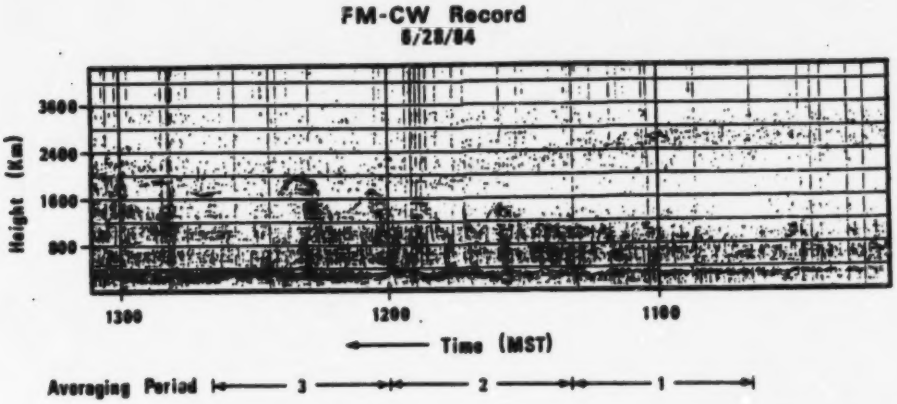

Figure 2.7.--Time-height cross section of echo power from the vertically pointing FM-CW radar located near the BAO tower on 28 June 1984.

BEST COPY AVAILABLE

The individual point targets that constitute this layer are resolvable by both the FM-CW and the X-band radar and are presumably from a layer of insects descending at about 0.1 m/s. This is consistent with the mean vertical motions observed at this height for the 80° elevation data from radar C.

The descending layer is apparent in the 35° elevation data but not the 80° data from radar C. Presumably this is because of the three-to-one sample volume ratio between the two elevations. The lower elevation data have a larger sample volume because of the increased range to the layer, and therefore we are three times more likely to find a scatterer in its sample volume.

The FM-CW record also shows a more uniform low-level echo gradually increasing with height near the level presumed from the three soundings to be the top of the mixed layer. Below the 400-m level is a strong layer increasing only slightly in height, which is most likely the top of the superadiabatic layer. The scattering mechanism for both of these FM-CW layers is the refractive index scatter mechanism discussed in Sec. 1.

The X-band radar had continuous echo within the mixed layer for the 2-h period, but the scattering must have been from particulates for reasons discussed earlier in this section. The high density of particles in the mixed layer resulted in a continuous echo because the radar was unable to resolve the individual scatterers.

A perusal of the time-height data and the 40-min profile data for each radar indicates occasional differences of as great as 1 m/s between radar estimates, although on the average they are in much better agreement than this as shown later in this section. Because the demonstrated accuracy of the method (see Sec. 2.2) is about an order of magnitude better than this, we conclude that spatial variability in the CBL is the cause of the observed differences.

The elevation angles presented here, 35° and 80°, were selected to give accurate estimates of the horizontal and vertical wind components as well as to demonstrate the ability of the technique to estimate the covariances $\overline{u'w'}$, and $\overline{w'^2}$ The scan-to-scan repeatability in the cross sections is reason for optimism. Note that the apparent internal consistency for the horizontal components is better for the 35° elevation data than for the 80° data (see the

BEST COPY AVAILABLE

Appendix). This is the result of the larger spatial filtering inherent in the 35° elevation scan.

It should be noted that the component labeled w in all plots in the Appendix is actually the quantity w + R/2 DIV ctnθ, as discussed in Sec. 2.3, and can be correctly interpreted as the vertical velocity component only if the second term is negligible. Thus w represents the true vertical velocity for the 80 scans but not necessarily for the scans at 35° elevation. The average of w at all heights, at all three intervals, and for both radars when at 80° elevation is -0.16 ± 0.08 m/s. We can take this as a measure of the mean fall speed of the particulate scatterers, since over such an average the mean vertical air speed is expected to be near zero.

Table 2.2 summarizes the differences in horizontal wind components between radar measurements and tower measurements at the 300-m level. Each sample includes a 40-min average of either u or v, and the first four entries include radar measurements at 5°, 20°, 35°, and 50° elevation. For $\theta \leq 50°$, the entire sample of 46 indicates no bias between both the radars and the tower, i.e., $\overline{\Delta V}_H = 0$ m/s. This suggests that the particulates are good tracers of the air motion and have negligible self-induced motion. As expected, the horizontal wind components are less accurately measured at 80°. The 50° elevation scans for the first interval of the D radar data were not processed, resulting in the u and v components for this period not being

Table 2.2—Comparison of radar measurements and tower measurements of horizontal wind components, and the standard deviation of the differences (σ), shown as mean difference ($\overline{\Delta V}_H$)

	$\overline{\Delta V}_H$ (m/s)	σ (m/s)	n (samples)
BAO - C radar, $\theta \leq 50°$	0.18	0.47	24
BAO - D radar, $\theta \leq 50°$	-0.20	0.60	22
BAO - both radars, $\theta \leq 50°$	0.00	0.57	46
C radar - D radar, $\theta \leq 50°$	-0.38	0.67	22
BAO - both radars, $\theta = 80°$	-0.22	0.94	12

Note: All three 40-min periods are included, and u and v components are included as separate samples.

BEST COPY AVAILABLE

included. The modest difference between the two radars is attributed to spatial inhomogeneity over the radar separation of 12 km.

With regard to the turbulence profiles in the Appendix, only the vertical velocity variance, $\overline{w'^2}$ taken at 80° elevation will be mentioned here. In general these profiles show a maximum just below the middle of the CBL and smaller values near the surface and near the capping inversion. Profiles from both radars illustrate the growth of the mixed layer and increased turbulence, especially near the midpoint, as the mixed layer heats up. Similar to the differences observed in the mean wind components, differences between the two radar measurements of $\overline{w'^2}$ and other second-order quantities must be attributed to spatial inhomogeneity rather than measurement error, which is expected to be an order of magnitude smaller than differences seen in these observations.

2.5 Summary and Conclusions

Vertical profiles of wind and turbulence stress components were computed from velocity-versus-azimuth data taken by the two NOAA/WPL X-band radars for a 2-h period when they were in the conical scan mode. The naturally occurring particulates often found in the CBL in Colorado were used as tracers of the air motion. For that time, signal strength was adequate to have produced wind profiles to heights of 3 km, about twice the depth of the CBL, although an overly conservative error threshold generally limited the data shown here to about 1.5 km.

An examination of data from a high-resolution, vertically pointing FM-CW radar indicated that the echo above the capping inversion was the result of many separable point targets, presumably insects. The Doppler radars indicated that the mean fall speed of these targets was 0.16 m/s ± 0.08 m/s. Because of the inherent accuracy of the method, horizontal velocity estimates from each radar differed occasionally by about 1 m/s, which is attributed to spatial inhomogeneity even though the radars were 12 km apart and the cloud-free boundary layer was seemingly undistrubed during this period.

Data shown in this section illustrate that microwave Doppler radars such as Firefinder can measure wind profiles in the convective boundary layer and that sometimes suitable wind tracers can be found above the capping inversion.

BEST COPY AVAILABLE

Very accurate wind measurements can be made in short dwell times because the scattering signal from particulate wind tracers can be much greater than the signal from refractive turbulence.

2.6 References

Browning, K.A., and R. Wexler, 1968. The determination of kinematic properties of a wind field using Doppler radar. J. Appl. Meteorol., 7, 105-113.

Hardy, K.R., and I. Katz, 1969. Probing the clear atmosphere with high power, high resolution radars. Proc. IEEE, 27, 468-480.

Kropfli, R.A., I. Katz, T.G. Konrad, and E.B. Dobson, 1968. Simultaneous radar reflectivity measurements and refractive index spectra in the clear atmosphere. Radio Sci., 3 (new series), 991-994.

Mathews, J., and R.L. Walker, 1965. Mathematical Methods of Physics. W.A. Benjamin, Inc., New York, 475 pp.

Pasqualucci, F., B.W. Bartram, R.A. Kropfli, and W.R. Moninger, 1983. A millimeter wavelength dual-polarization Doppler radar for cloud and precipitation studies. J. Clim. Appl. Meteorol., 758-765.

Schaefer, G.W., 1976. Radar observations of insect flight. Proc., Symposium of Royal Entomological Society of London, 157-197.

Wilson, D.A., 1970. Doppler radar studies of boundary layer wind profiles and turbulence in snow conditions. Proceedings, 14th Radar Meteorology Conf., American Meteorological Society, Boston, MA, 191-196.

BEST COPY AVAILABLE

3. STATISTICAL ANALYSIS OF THE HEIGHT COVERAGE OF 50-, 405-, AND 915-MHz RADAR WIND PROFILERS

The Wave Propagation Laboratory has operated a small research network of radar wind Profilers in Colorado for about 2 years (Strauch et al., 1984). Data archiving procedures have been in place for about 1 year, and we are able to use this data base to evaluate the performance of the radars.

One of the prime concerns of potential wind Profiler users is how often and how long wind measurements are lacking at a given height. Since these "outages" constitute an important part of the "performance" of the wind Profilers, they are calculated at three different radar frequencies, 50, 405, and 915 MHz (wavelengths of 6, 0.74, and 0.33 m) at monthly intervals to determine both the number of outages at each frequency and annual variations in outages. This study on the monthly performance of the wind Profilers (i.e., measurements or no measurements at various heights) is based on the more recent archived data from the Colorado Wind Profiler network. We do not consider how well the winds are measured. Tables 3.1, 3.2, and 3.3 list the parameters of the Colorado network radars.

Table 3.1—Parameters of the 50-MHz Radar

Radar		
Frequency	49.8 MHz	
Authorized bandwidth	0.4 MHz	
Peak power	30 kW	
Average power	400 W	
Pulse width	3, 9 μs	
Pulse repetition period	238.67, 672 μs	
Antenna aperture	50 m × 50 m	
Antenna pointing	15° off-zenith to north and east (2 antennas)	
Antenna type	fixed phase array of colinear-coaxial dipoles	
Two-way beamwidth	5°	
Data Processing	**3-μs pulse**	**9-μs pulse**
Time domain averaging	419 pulses	124 pulses
Spectral averages	8	16
Maximum radial velocity	±15.05 m/s	±18.06 m/s
Spectral resolution (64 points)	0.47 m/s	0.56 m/s
Height Sampling		
First height	1.7 km	2.6 km
Height spacing	290 m	870 m
Number of heights	24	18

BEST COPY AVAILABLE

Table 3.2--Parameters of the 915-MHz radar

Radar			
Frequency	915 MHz		
Maximum bandwidth	2 MHz		
Peak power	5.6 kW		
Duty cycle	<25%		
Antenna aperture	≈10 m x 10 m		
Antenna pointing	zenith, 15° off-zenith to north and east		
Antenna type	offset paraboloidal reflector with offset horn feeds		
Two-way beamwidth	1.7°		
System noise temperature	240 K		
Data Processing	**1-μs pulse**	**3-μs pulse**	**9-μs pulse**
Pulse repetition period	50 μs	64 μs	110 μs
Average power	110 W	260 W	450 W
Time domain averaging	136 pulses	80 pulses	46 pulses
Spectral averaging	8 spectra	32 spectra	32 spectra
Maximum radial velocity	———	12.02 m/s	———
Spectral resolution (64 points)	———	0.375 m/s	———
Height Sampling			
First height	1.06 km	1.64 km	2.7 km
Height spacing	100 m	290 m	870 m
Number of heights	24	24	18

Table 3.3--Parameters of the 405-MHz radar

Radar			
Frequency	405.25 MHz		
Authorized bandwidth	1.00 MHz		
Peak power	30 kW		
Average power	1.3 kW maximum		
Pulse width	1, 3, 9 μs		
Pulse repetition period	100, 150, 300 μs		
Antenna aperture	9 m × 9 m		
Antenna pointing	15° off-zenith to north and east		
Antenna type	phased array of Yagi-Uda elements		
Two-way beamwidth	4.3°		
Data Processing	**1-μs pulse**	**3-μs pulse**	**9-μs pulse**
Time domain averaging	120 pulses	75 pulses	35 pulses
Spectral averages	8	16	24
Maximum radial velocity	±15.41 m/s	±16.44 m/s	±17.62 m/s
Spectral resolution (64 points)	0.48 m/s	0.51 m/s	0.55 m/s
Height Sampling			
First height	0.4 km	2.4 km	4.0 km
Height spacing	100 m	290 m	870 m
Number of heights	24	24	14

BEST COPY AVAILABLE

3.1 Radar Sensitivity Comparisons

The three radars operate with pulse widths of 3 and 9 μs. We can compare the sensitivities of the various radars and their modes using the radar equations developed in Sec. 1.

First, when we compare separate pulse widths for the same radar, we find relative sensitivity is proportional to $[\Delta R \overline{P_t} \sqrt{\bar{T}_o}]$. For our radars the 9-μs mode is more sensitive than the 3-μs mode as shown below:

50 MHz, +6.4 dB
405 MHz, +7.3 dB
915 MHz, +7.1 dB

These relative sensitivity values are important for evaluating the performance of a given radar with different pulse widths.

Second, when we compare the three radars and assume scattering from homogeneous, isotropic turbulence in the optically clear atmosphere with the radar half-wavelength in the inertial subrange, then relative sensitivity is proportional to

$$\frac{\bar{P}_t A_e \Delta R \sqrt{\bar{T}_o} \lambda^{1/6}}{(T_{op}) L_T L_F L_R} .$$

For the 9-μs pulse mode, the 50-MHz radar is 6.5 dB more sensitive than the 405-MHz radar, and 7.0 dB more sensitive than the 915 MHz radar. These numbers are important in comparing the performances of the radars.

3.2 Archiving

The radar signals are sampled at 2- and 6-μs intervals for radar pulse widths of 3 and 9 μs; the UHF radars (405 and 915 MHz) use a 1-μs-width pulse as well. Twelve wind profiles are measured per hour for each sample spacing and are filtered by a random sample consensus window (Fischler and Bolles, 1981); those samples passing the consensus test (at least four of the twelve) are averaged together. If less than four are within the consensus window, a wind vector is not calculated; it is assumed that the twelve measurements are so inconsistent that they can be regarded as random noise. This technique

BEST COPY AVAILABLE

eliminates most of the random velocities that occur in the Doppler processing when there is an inadequate signal.

3.3 Profiler Outages

To compute statistics of the times no measurements were made at a specific height, we used the data base available from the Stapleton (Denver) 915-MHz, the Platteville 405-MHz, and the Fleming 50-MHz wind Profilers.

Figure 3.1 shows a sample of the time-height history of the Platteville 405-MHz Profiler for the 1-μs pulse mode. Each vertical dash represents a measurement. If there was no measurement at a particular height and time, no symbol is plotted. The periods that show no data at all are due to equipment outages such as power failures, and these outages are not included in the statistics.

Figures 3.2 and 3.3 are time-height plots of the 405-MHz wind Profiler performance in the middle (3-μs) and the high (9-μs) modes. Between day 4 and 7 at 9 km we see fewer outages in the 9-μs mode than in the 3-μs mode. In this particular example, the decrease in the outages is due to an increase in sensitivity (~7 dB) of the 9-μs mode over the 3-μs mode. Where both modes show outages, we know there is insufficient Bragg scattering from refractive turbulence in the pulse volume at one-half the radar wavelength; whether the problem relates to an increase in inner scale we cannot say. The answer depends on the "depth of fade," and since there is no available signal, these data do not give the answer.

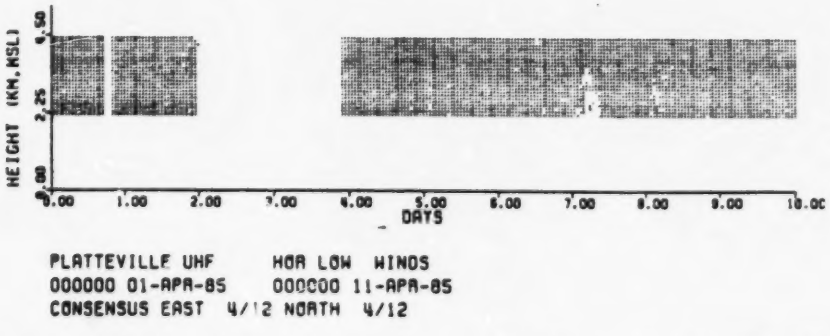

Figure 3.1.--Height-time display of the 1-μs mode for the Platteville 405-MHz wind Profiler. Vertical dashes indicate that there was a wind measurement at that time and height.

BEST COPY AVAILABLE

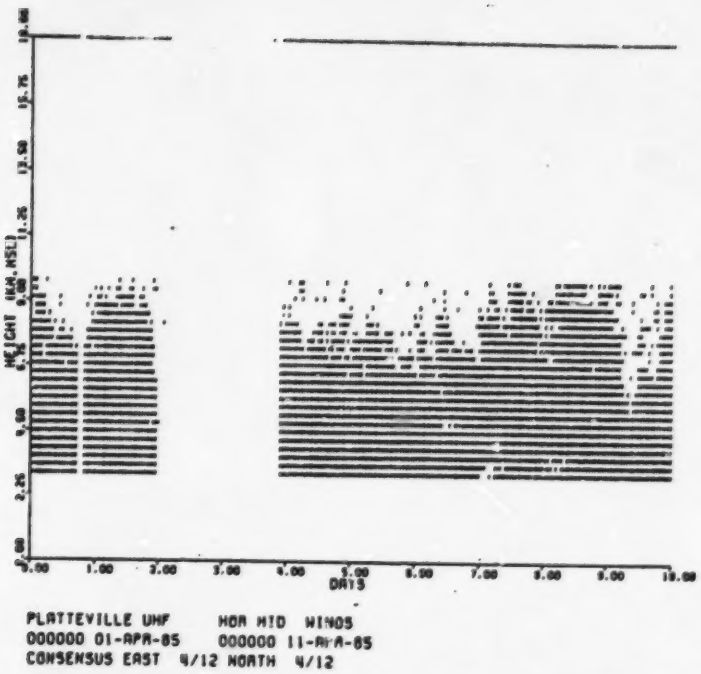

Figure 3.2.--Height-time display of the 3-μs mode for the Platteville 405-MHz wind Profiler. Vertical dashes indicate that there was a wind measurement at that time and height.

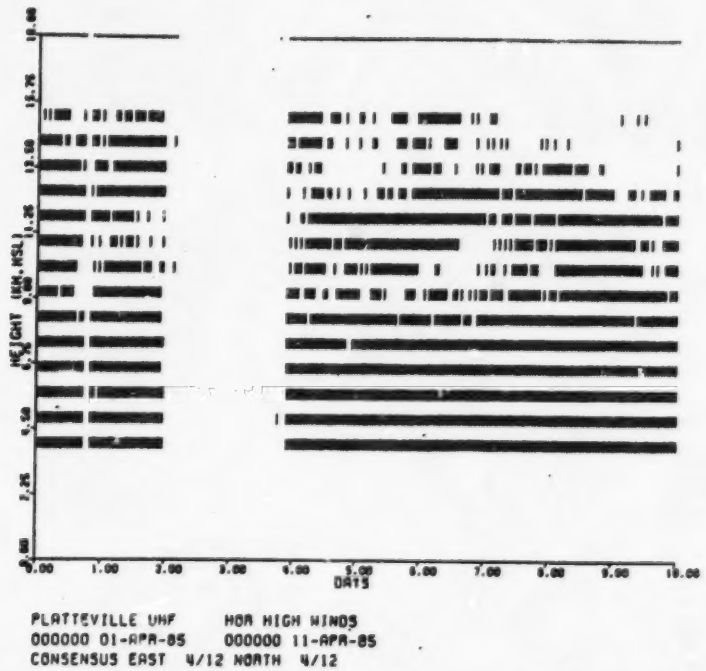

Figure 3.3.--Height-time display of the 9-μs mode for the Platteville 405-MHz wind Profiler. Vertical dashes indicate that there was a wind measurement at that time and height.

BEST COPY AVAILABLE

3.4 Distribution of Outages

The distribution of outage lengths was computed as a function of time and height. Figure 3.4 shows a sample of the July statistics for the 3- and 9-μs modes between 9 and 10 km at 915 MHz. In the 3-μs mode the longest outage length was about 50 h, and at 9 μs the longest was 10 h, indicating that the 7-dB increase in sensitivity decreased the maximum outage time by a factor of 5 for this height and month. Similar results are shown in Fig. 3.5 for January 1985; very little difference is seen in the performance of the 915-MHz radar for the summer and winter months.

The July statistics for the 50-MHz Profiler (Fig. 3.6) show that the maximum outage at 10 km was about 50 h in the 3-μs mode. Increasing the sensitivity by 7 dB (9-μs mode) decreased the maximum outage length to 4 h. In January 1985 (Fig. 3.7), the maximum outage length for the 50-MHz radar (between 9 and 10 km) was 30 h in the 3-μs mode, and 1 h at 9 μs, reflecting a noticeable improvement in performance in both modes in a winter month.

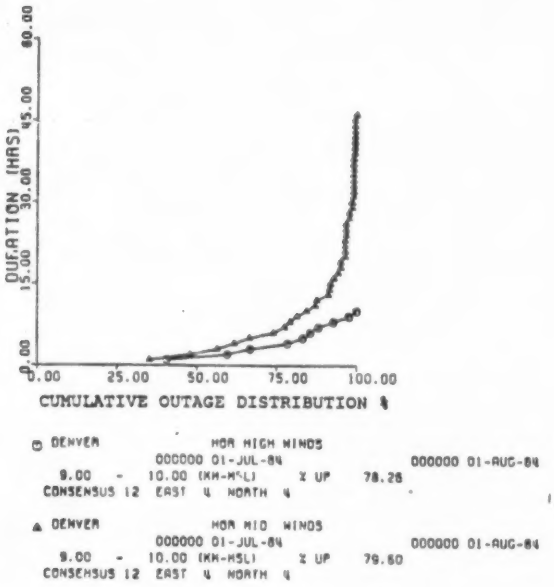

Figure 3.4.--Distribution of outage durations for the 3-μs (triangles) and 9-μs (circles) modes at 915 MHz. Data were taken between 9 and 10 km in July 1984.

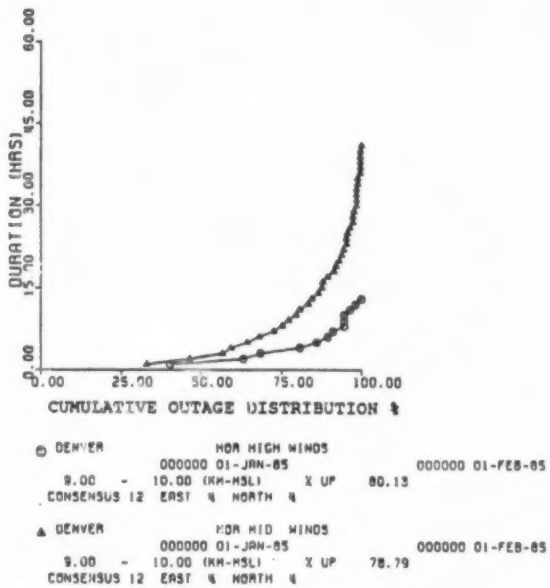

Figure 3.5.--Distribution of outage durations for the 3-μs (triangles) and 9-μs (circles) modes at 915 MHz. Data were taken between 9 and 10 km in July 1985.

BEST COPY AVAILABLE

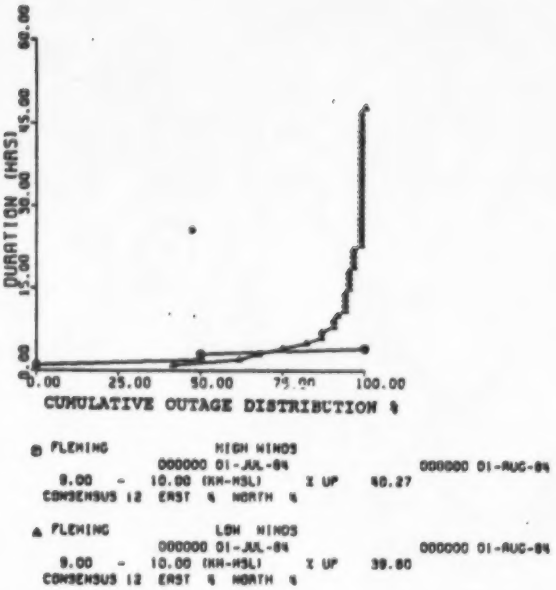

Figure 3.6.--Distribution of outage durations for the 3-μs (triangles) and 9-μs (circles) modes at 50 MHz. Data were taken between 9 and 10 km in July 1984.

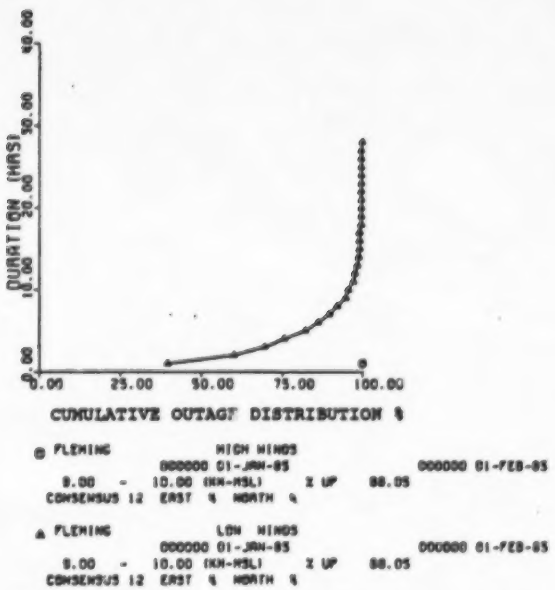

Figure 3.7.--Distribution of outage durations for the 3-μs (triangles) and 9-μs (circles) modes at 50 MHz. Data were taken between 9 and 10 km in January 1985.

When we compare the outages at 915 MHz (Fig. 3.4) and at 50 MHz (Fig. 3.6) for the same month, we see dramatic differences between the 3-μs and 9-μs modes for the two radars, even though the increase in radar sensitivity between the two modes was roughly the same for the two radars (~7 dB). At 10 km, the 50-MHz 3-μs mode had a maximum outage in excess of 50 h; at 9 μs, the maximum outage was reduced to 4 h. Since both the 915-MHz and 50-MHz Profilers were in the same geographical area, we infer that this dramatic difference in the change in performance between 3 and 9 μs is due to the difference in the distribution function of the backscattering cross section at the two frequencies.

The data base for the 405-MHz wind Profiler at Platteville starts in January 1985. Figure 3.8 shows outage duration distribution for January 1985 at the 10-km height. With this radar the maximum outage duration was 31 h in the 3-μs mode and only 5 h in the 9-μs mode.

BEST COPY AVAILABLE

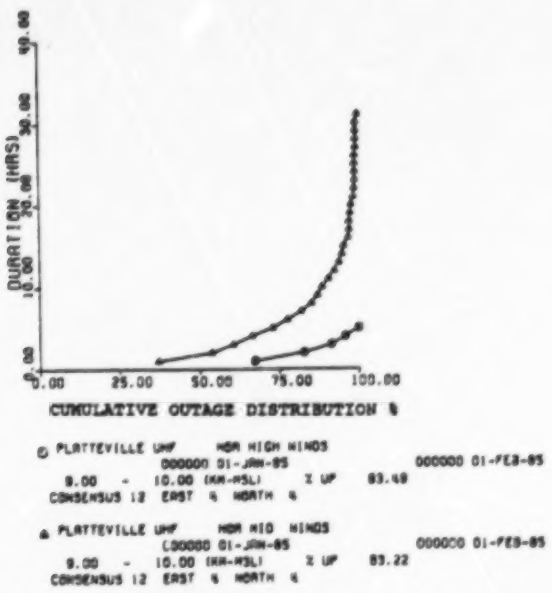

Figure 3.8.--Distribution of outage durations for the 3-μs (triangles) and 9-μs (circles) modes at 405 MHz. Data were taken between 9 and 10 km in January 1985.

3.5 Height of Outages

One of the statistics used to measure the performance of the Profilers involved the height at which the Profiler was "down" (no wind data, given that the radar is operating) for 3 or more consecutive hours. Samples of these down-time statistics for January 1985 at the three frequencies are shown in Figs. 3.9, 3.10, and 3.11. The 50-MHz wind Profiler at Fleming (Fig. 3.9) had no outages to 6 km in either the 3- or 9-μs mode, and none until almost 14 km in the 9-μs mode. In comparison, the 405-MHz (Fig. 3.10) Profiler had outages starting at 6 km in the 3-μs mode, and at 9 km in the 9-μs mode; the 915-MHz Profiler (Fig. 3.11) had outages starting at a little over 5 km in the 3-μs mode and at 6 km in the 9-μs mode.

To report on all the monthly statistics in this way would be too detailed, and so we plotted the lowest height for the different modes where the probability of an outage for 3 or more consecutive hours reached 0.1, based on monthly data. These statistics are shown in Fig. 3.12 for the Fleming 50-MHz, in Fig. 3.13 for the Platteville 405-MHz, and in Fig. 3.14 for the Denver 915-MHz wind Profilers as a function of month. The top of the dark area in the

BEST COPY AVAILABLE

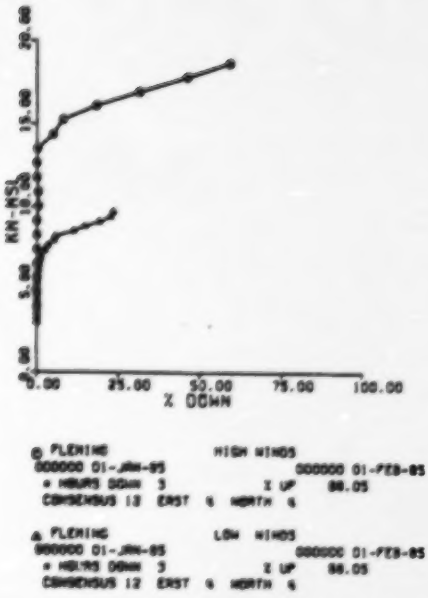

Figure 3.9.--Probability that an outage will last 3 or more hours vs. height at 50 MHz for the 3-μs (triangles and 9-μs (circles) modes based on January 1985 statistics.

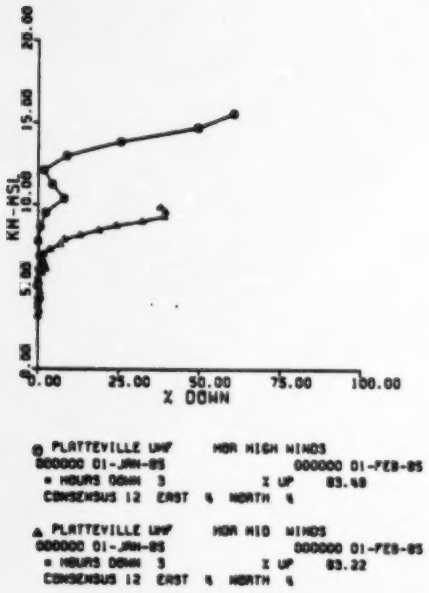

Figure 3.10.--Probability that an outage will last 3 or more hours vs. height at 405 MHz for the 3-μs (triangles and 9-μs (circles) modes based on January 1985 statistics.

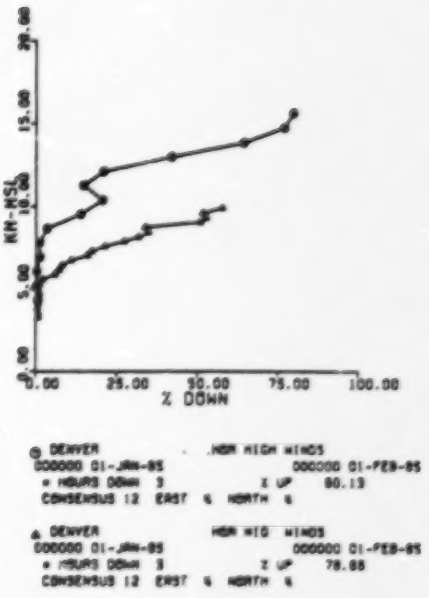

Figure 3.11.--Probability that an outage will last 3 or more hours vs. height at 915 MHz for the 3-μs (triangles) and 9μs (circles) modes based on January 1985 statistics.

BEST COPY AVAILABLE

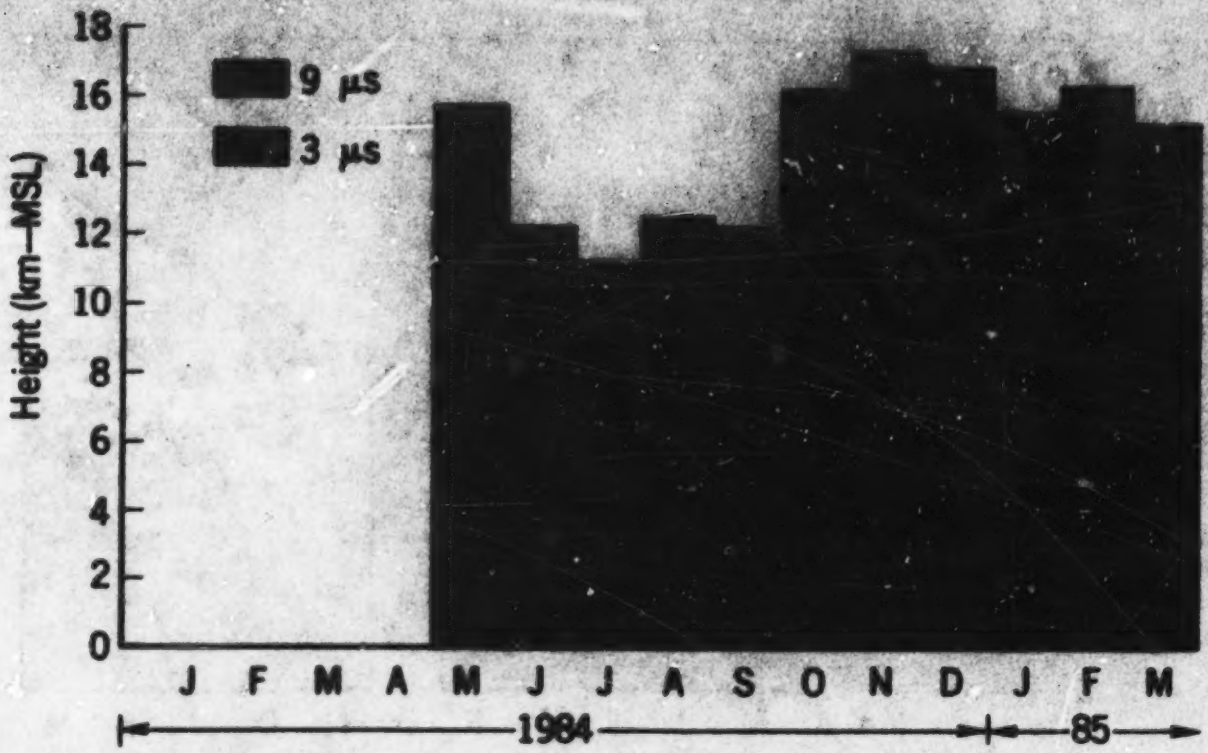

Figure 3.12.—Lowest height where the probability of an outage for > 3 consecutive hours is 0.1, for the 3- and 9-μs modes (50 MHz).

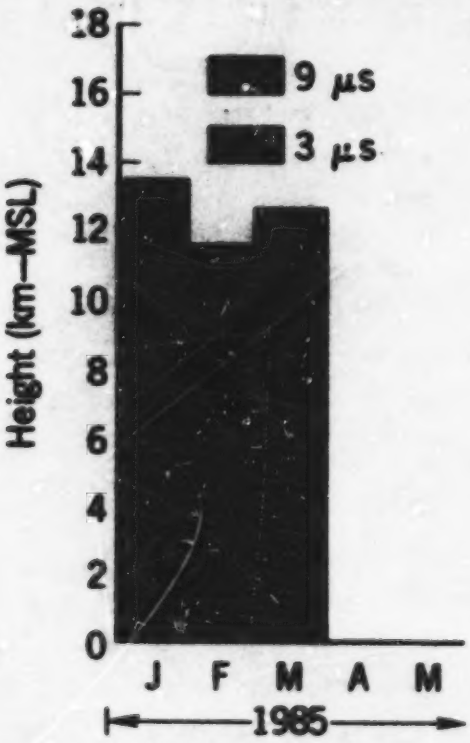

Figure 3.13.—Height where the probability of an outage for > 3 h increases to 10% of the time for the 3- and 9-μs modes (405 MHz).

BEST COPY AVAILABLE

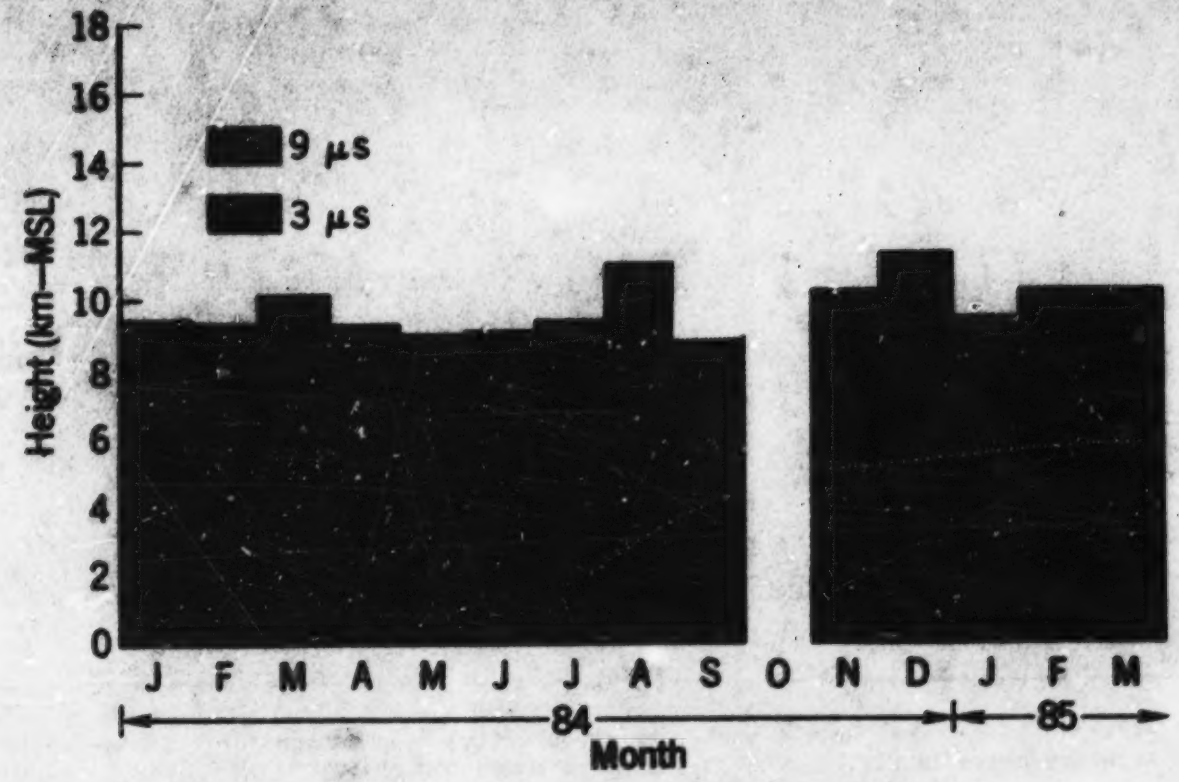

Figure 3.14.—Height where the probability of an outage for > 3 h increases to 10% of the time for the 3- and 9-μs modes (915 MHz).

bar graph denotes the lowest height at which the wind data with the 9-μs mode show an outage of 10% for > 3 h. The top of the lighter area is the lowest height at which the 3-μs mode has an outage of 10% for > 3 consecutive hours.

From Figs. 3.12 and 3.14, one can see there is much more seasonal variation in the performance of the 50-MHz system at Fleming than of the 915-MHz system at Denver. The Platteville 405-MHz system has not been operational long enough for assessment of its seasonal variation; for the 4 months that it has been operating, its performance has been between the 50- and 915-MHz Profilers.

We can examine the incremental gain in height performance of the Profilers with increased sensitivity as a function of frequency and month (Fig. 3.15) by comparing the 3- and 9-μs modes. The least seasonal change and improvement is at 915 MHz, and the largest seasonal variation and height change is at 50 MHz. The maximum change in height coverage at 915 MHz

BEST COPY AVAILABLE

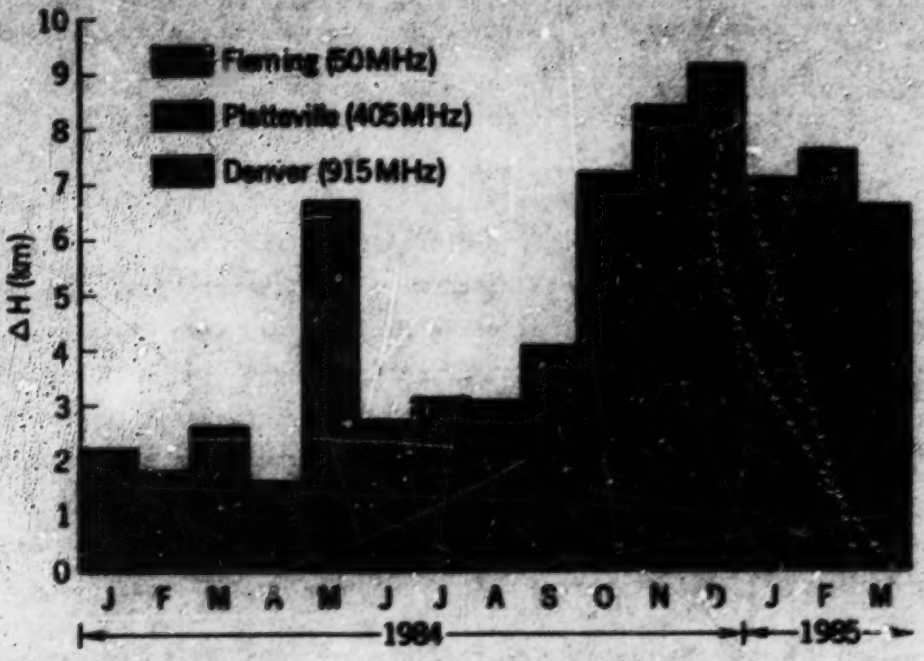

Figure 3.15.—Increase in height of wind measurements for the > 3 h outage probability of 0.1 for an increase in radar sensitivity. The sensitivity increase is obtained by increasing the pulse width from 3 to 9 μs.

occurred in December and was approximately 4 km. The maximum height change at 405 MHz was approximately 5.5 km; at 50 MHz it was slightly over 9 km.

Figure 3.16 summarizes the change in the average height improvement for the three radars. The 50 MHz radar has the greatest height change for the same increase in sensitivity, the 405 MHz the next greatest, and the 915 MHz

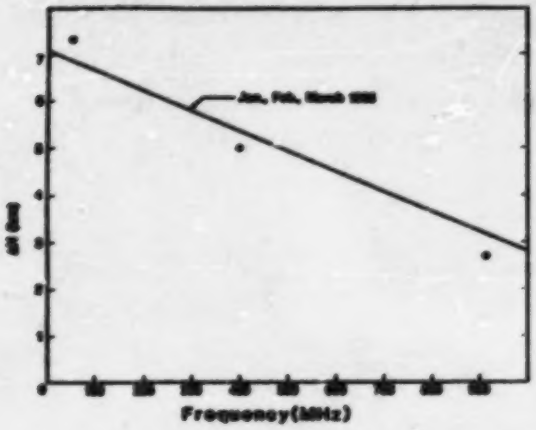

Figure 3.16.—Increase in height for a 3-consecutive-hour down time 10% of the time vs. frequency for January, February, and March 1985.

BEST COPY AVAILABLE

the least. The average increase in height performance for similar sensitivity changes (7 dB) was approximately 5 km at 50 MHz, approximately 4 km at 405 MHz, and approximately 2 km at 915 MHz.

3.6 Summary and Conclusions

On the basis of these archived wind profiles, we can estimate the radar frequency and sensitivity needed to achieve wind measurements to a given altitude. For example, the measurement of winds for some problems demands a transportable system with relatively low height coverage. The mobility requirement limits the maximum wavelength. Suppose a 5-m planar array (mechanical axis toward vertical) could be erected easily; then, since an antenna beamwidth of at most about 5° is desired, the longest wavelength would be about 35 cm. Such a radar with 500-W average power could provide wind data to 5-km altitude in nearly all-weather and to greater heights in most situations.

The outage statistics from the Colorado network data are for clear-air scattering because the data were obtained primarily in precipitation-free conditions, and because the lowest height where radar data are not available is higher than the altitude where precipitation particles or insects would be found. We cannot extend the height coverage of the longer wavelength radars to predict the clear-air coverage of Firefinder because we do not have a statistical description of the length of the inner scale. The trend to lower maximum altitude wind measurements with shorter wavelength is indicated clearly by the Colorado network, but experience with 10-cm radars with similar sensitivity indicates that the maximum altitude will decrease very abruptly as the wavelength decreases from 33 cm. This decrease is attributed to the increase in inner scale above the boundary layer. We should not expect Firefinder to achieve clear air wind measurements above the boundary layer.

3.7 References

Fischler, M.A., and R.C. Bolles, 1981. Random sample consensus: A paradigm for model fitting with applications to image analysis and automated cartography. Commun. Assoc. Comput. Mach., 24, 381-395.

BEST COPY AVAILABLE

Strauch, R.G., D.A. Merritt, K.P. Moran, K.B. Earnshaw, and D.W. van de Kamp, 1984. The Colorado wind-profiling network. J. Atmos. Oceanic Technol., 1, 37-49.

BEST COPY AVAILABLE

APPENDIX - DOPPLER RADAR PROFILES

BEST COPY AVAILABLE

Wind component cross-sections at 35° elevation: Period I.

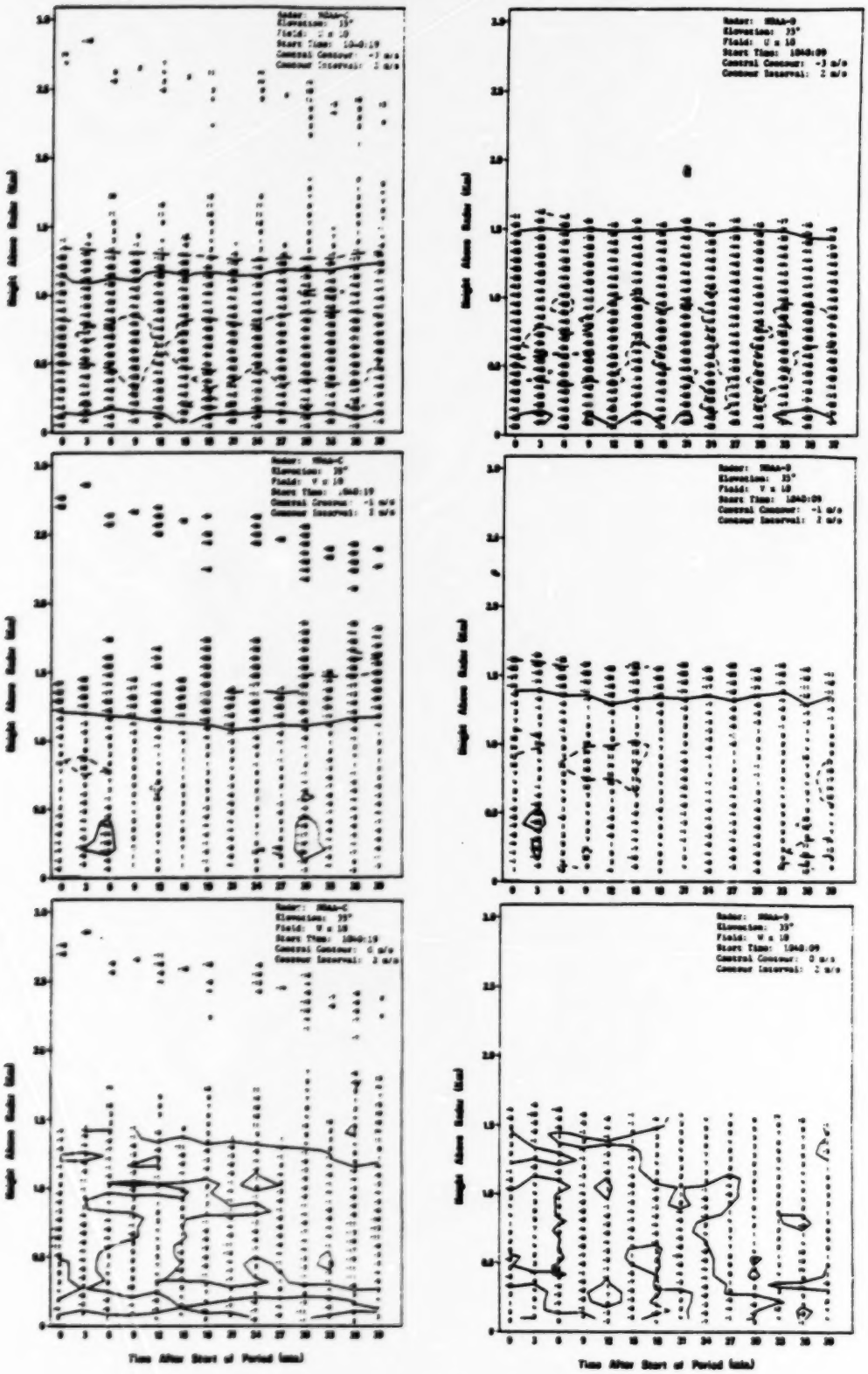

BEST COPY AVAILABLE

Wind component cross-sections at 35° elevation: Period II.

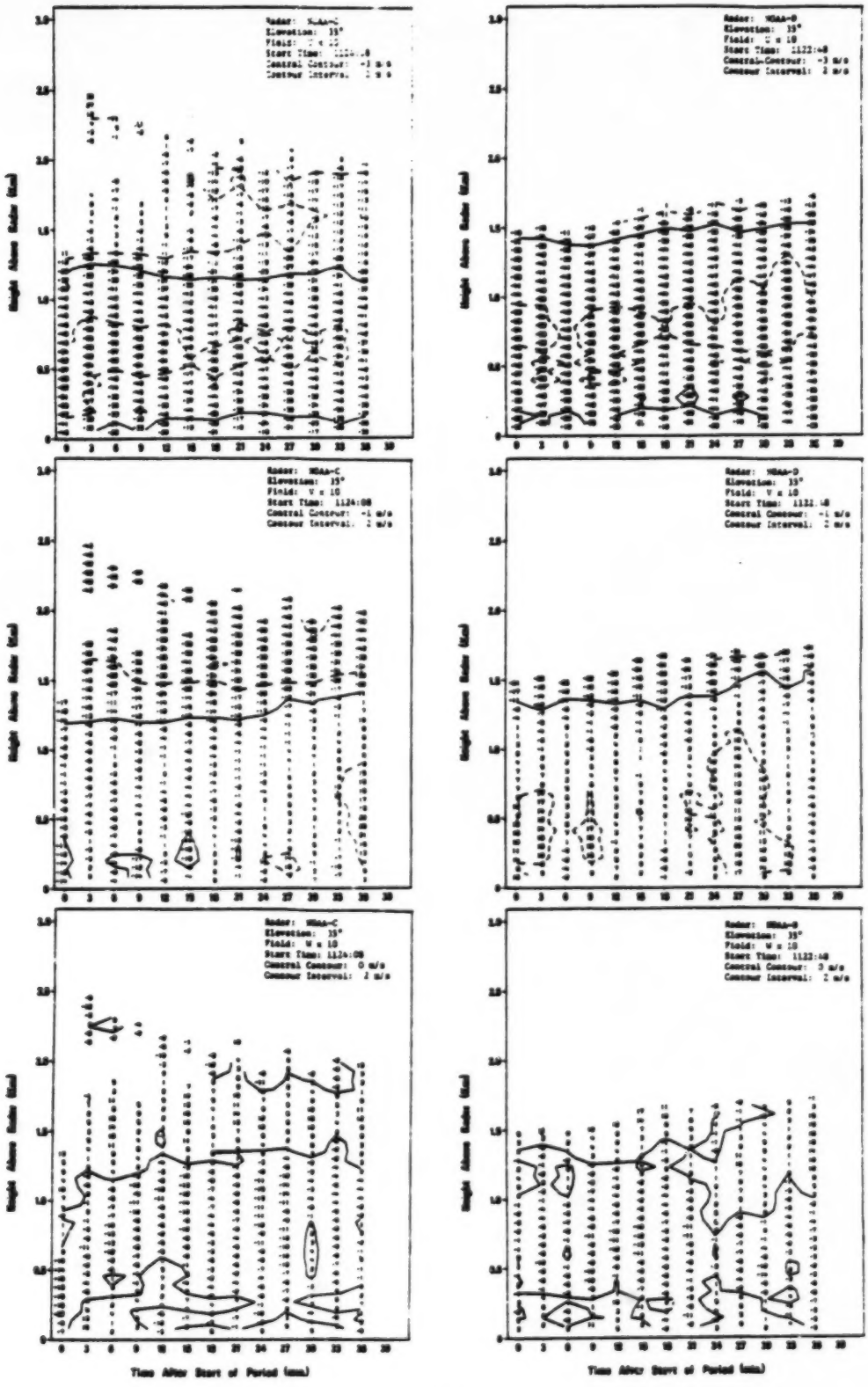

BEST COPY AVAILABLE

Wind component cross-sections at 35° elevation: Period III.

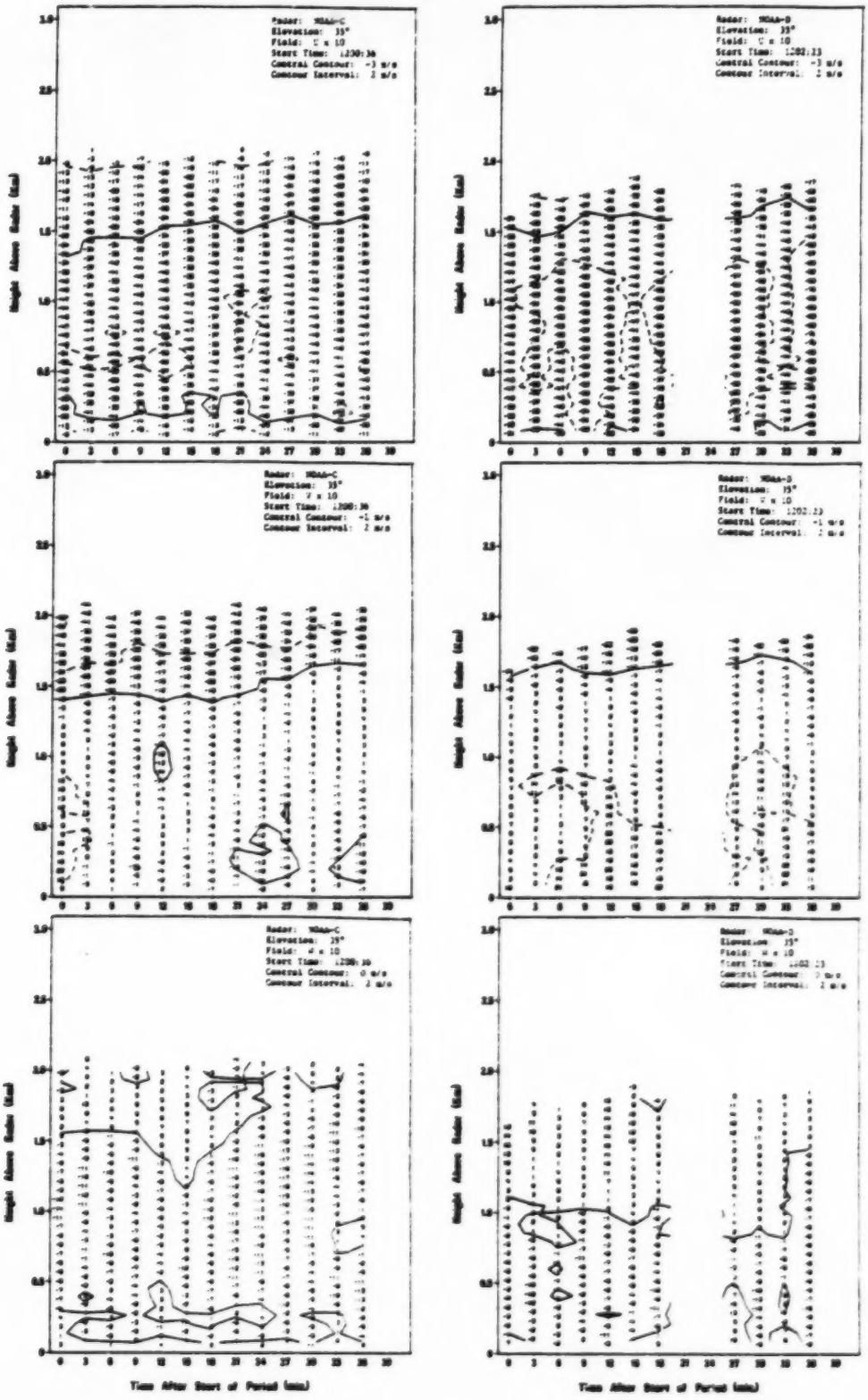

BEST COPY AVAILABLE

Mean wind profiles at 35° elevation.

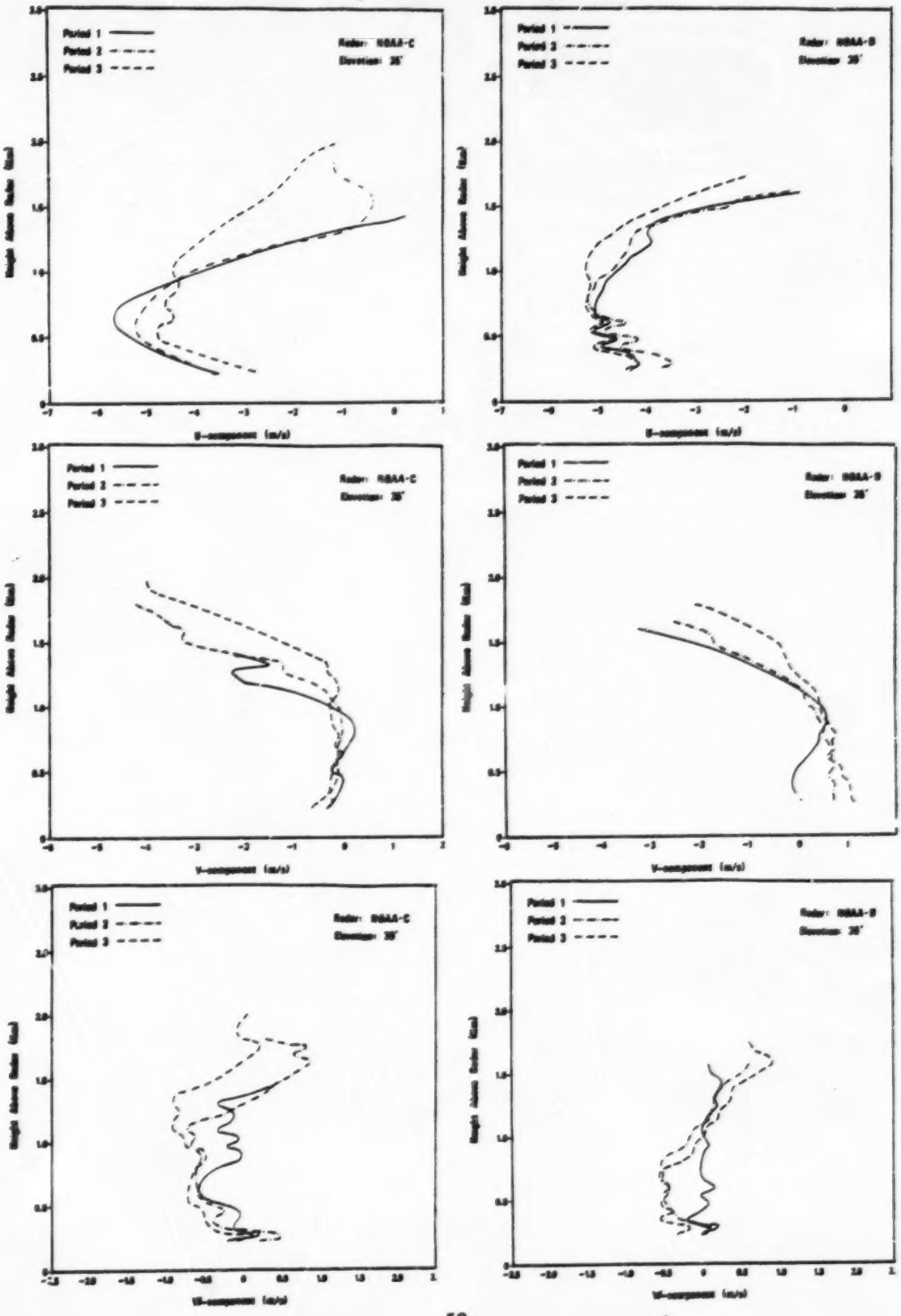

BEST COPY AVAILABLE

Wind component cross-sections at 80° elevation: Period I.

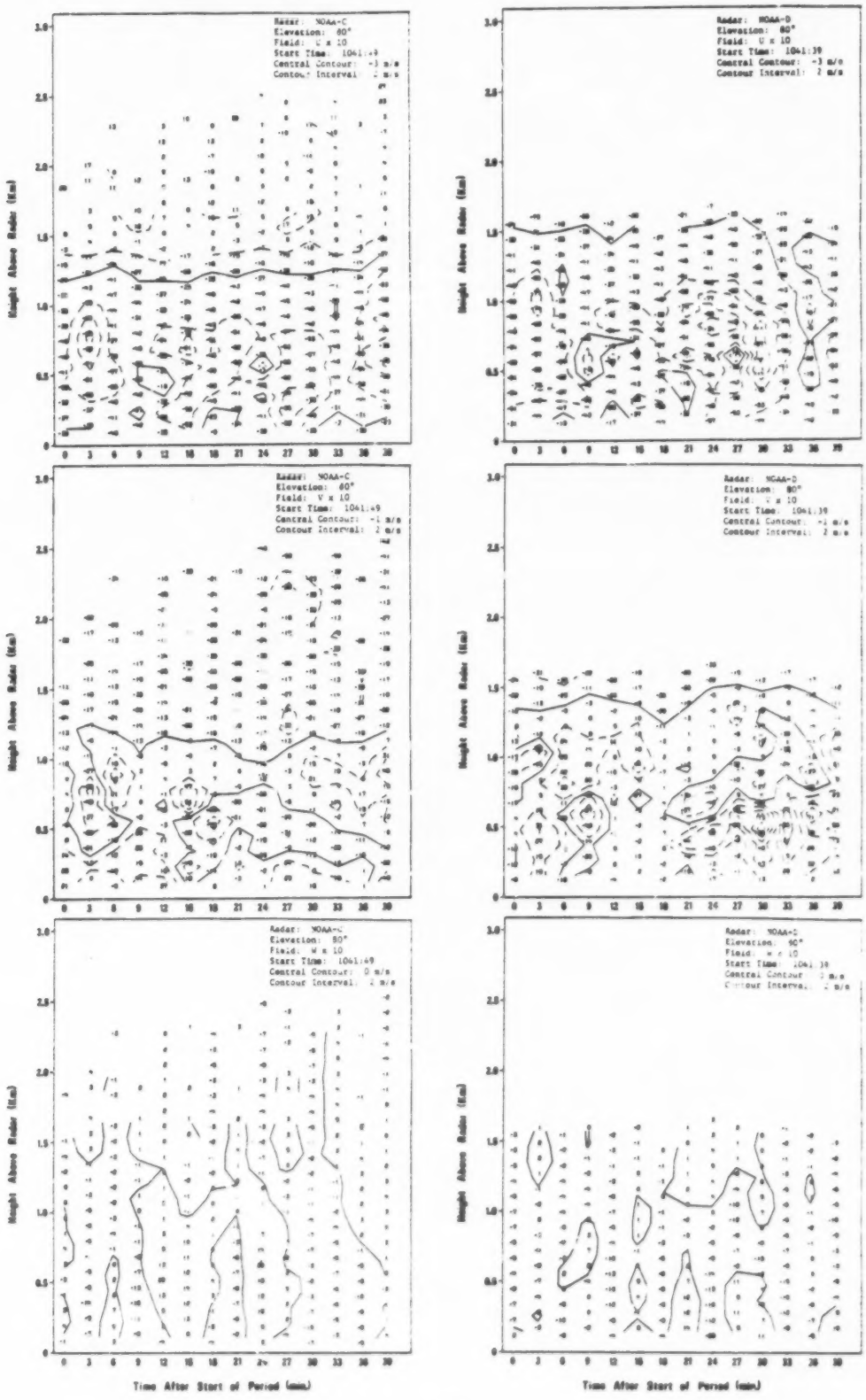

BEST COPY AVAILABLE

Wind component cross-sections at 80° elevation: Period II.

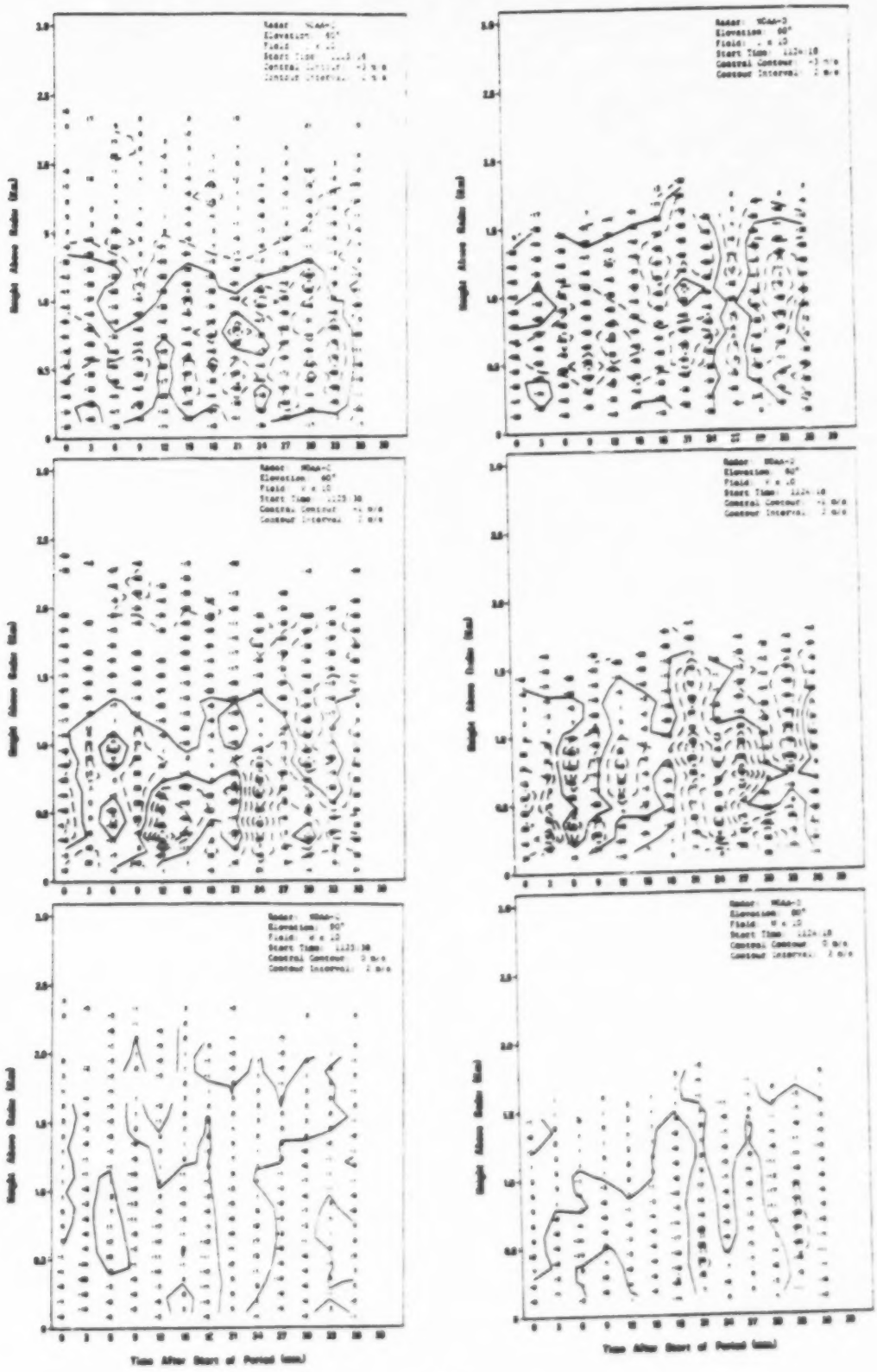

BEST COPY AVAILABLE

Wind component cross-sections at 80° elevation: Period III.

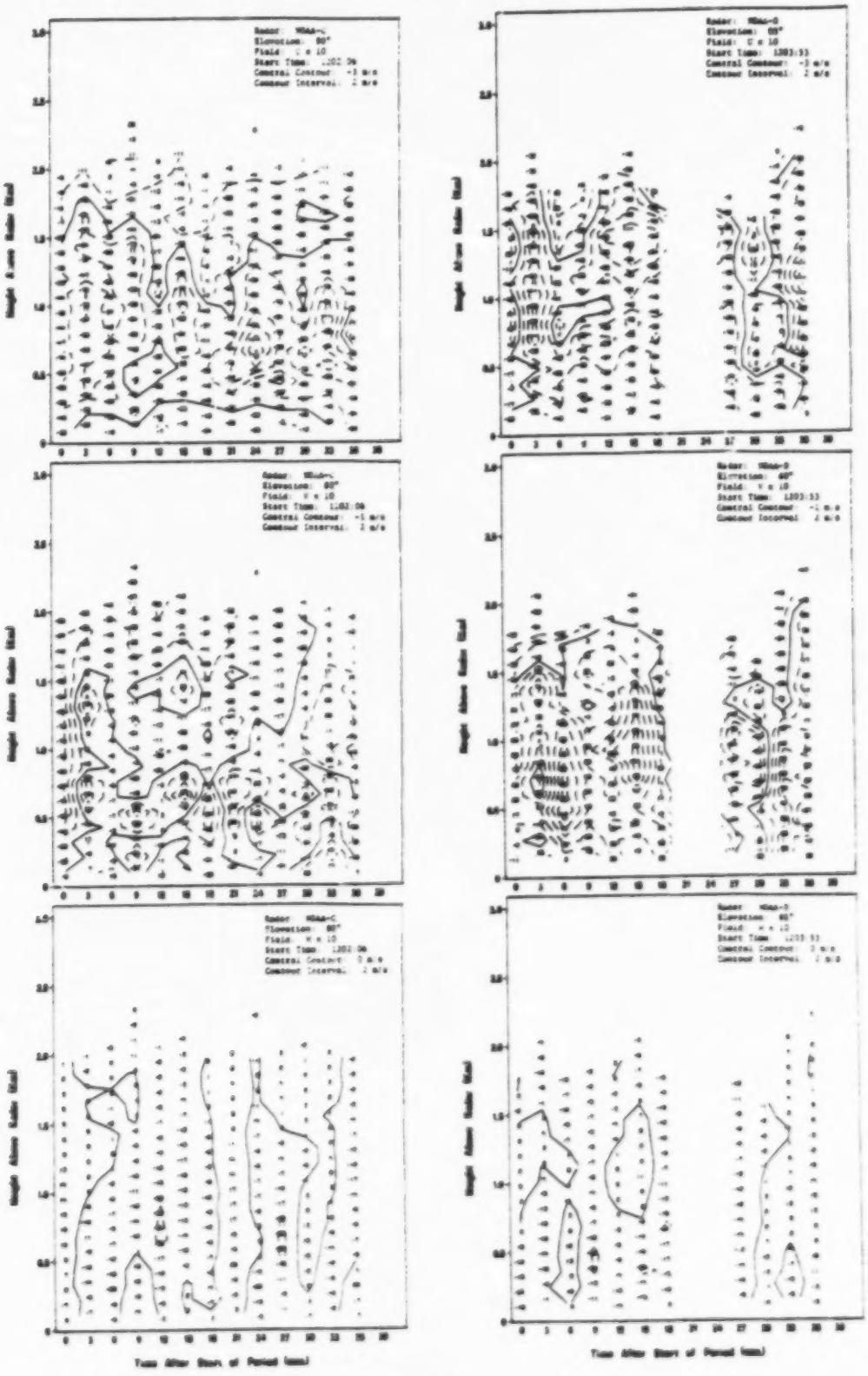

BEST COPY AVAILABLE

Mean wind profiles at 80° elevation.

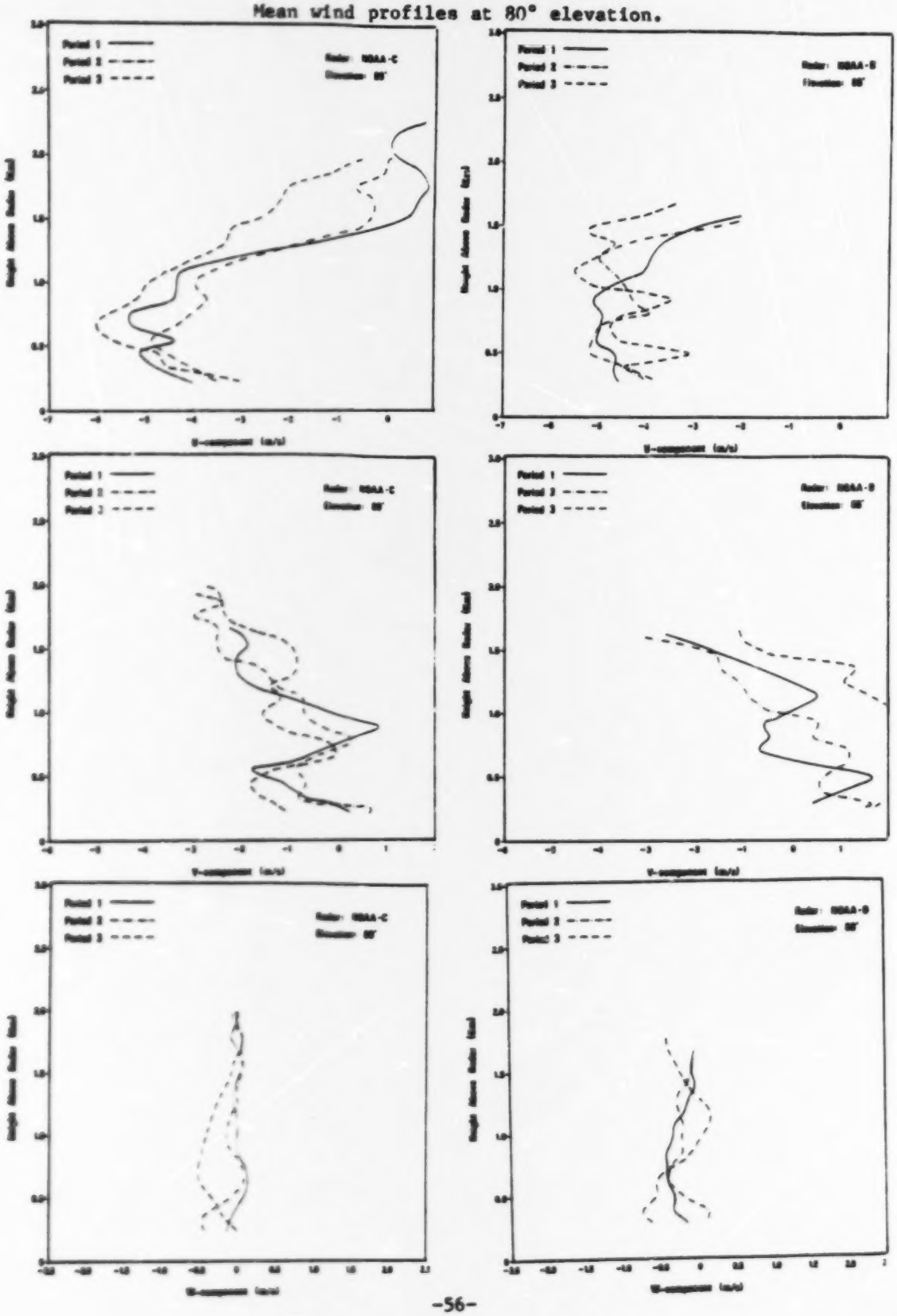

BEST COPY AVAILABLE

Reynolds stress cross-sections at 35° elevation: NOAA-C.

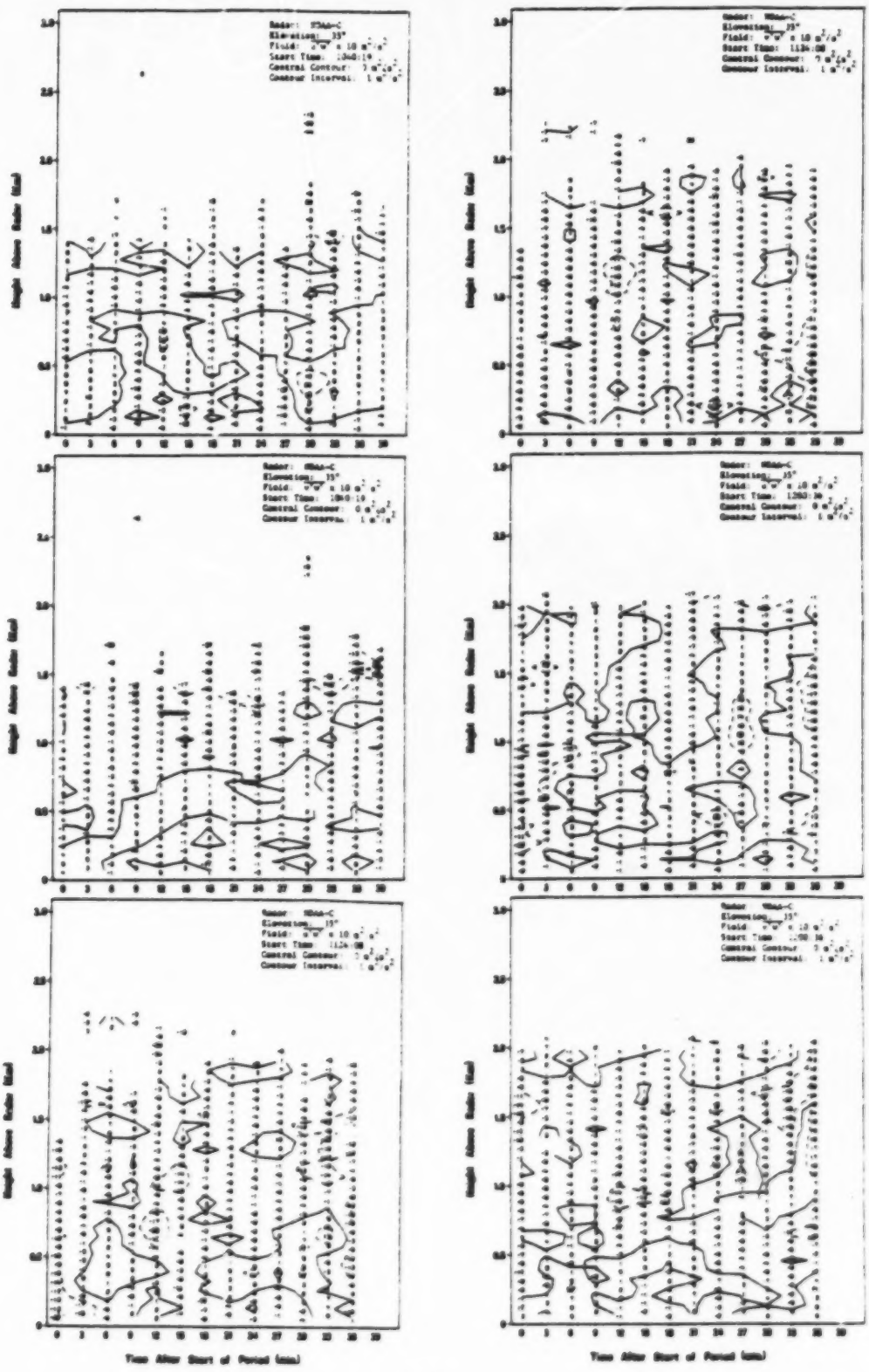

BEST COPY AVAILABLE

Reynolds stress cross-sections at 35° elevation: NOAA-D.

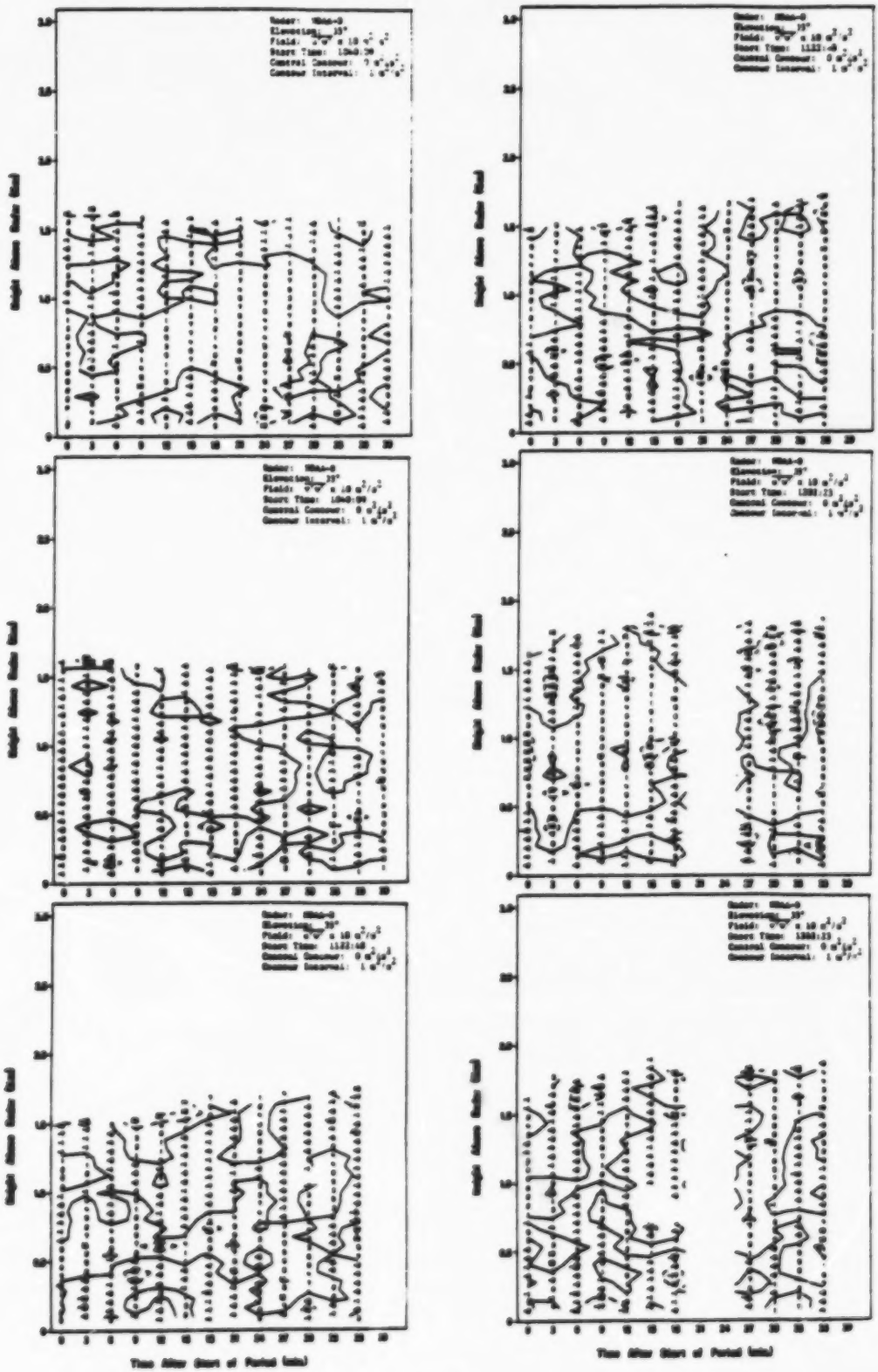

BEST COPY AVAILABLE

Reynolds stress profiles at 35° elevation.

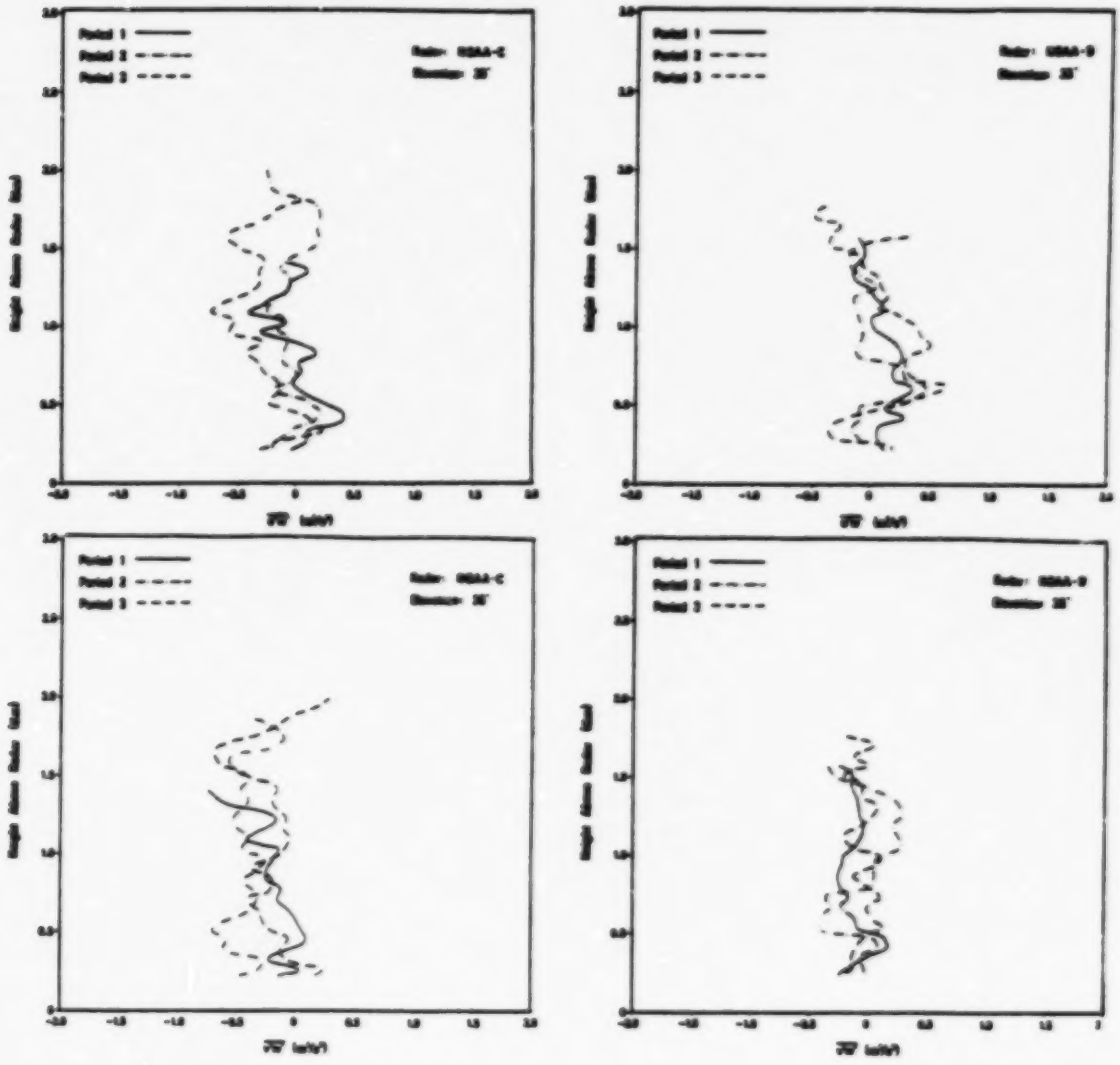

BEST COPY AVAILABLE

Vertical velocity variance cross-sections at 80°.

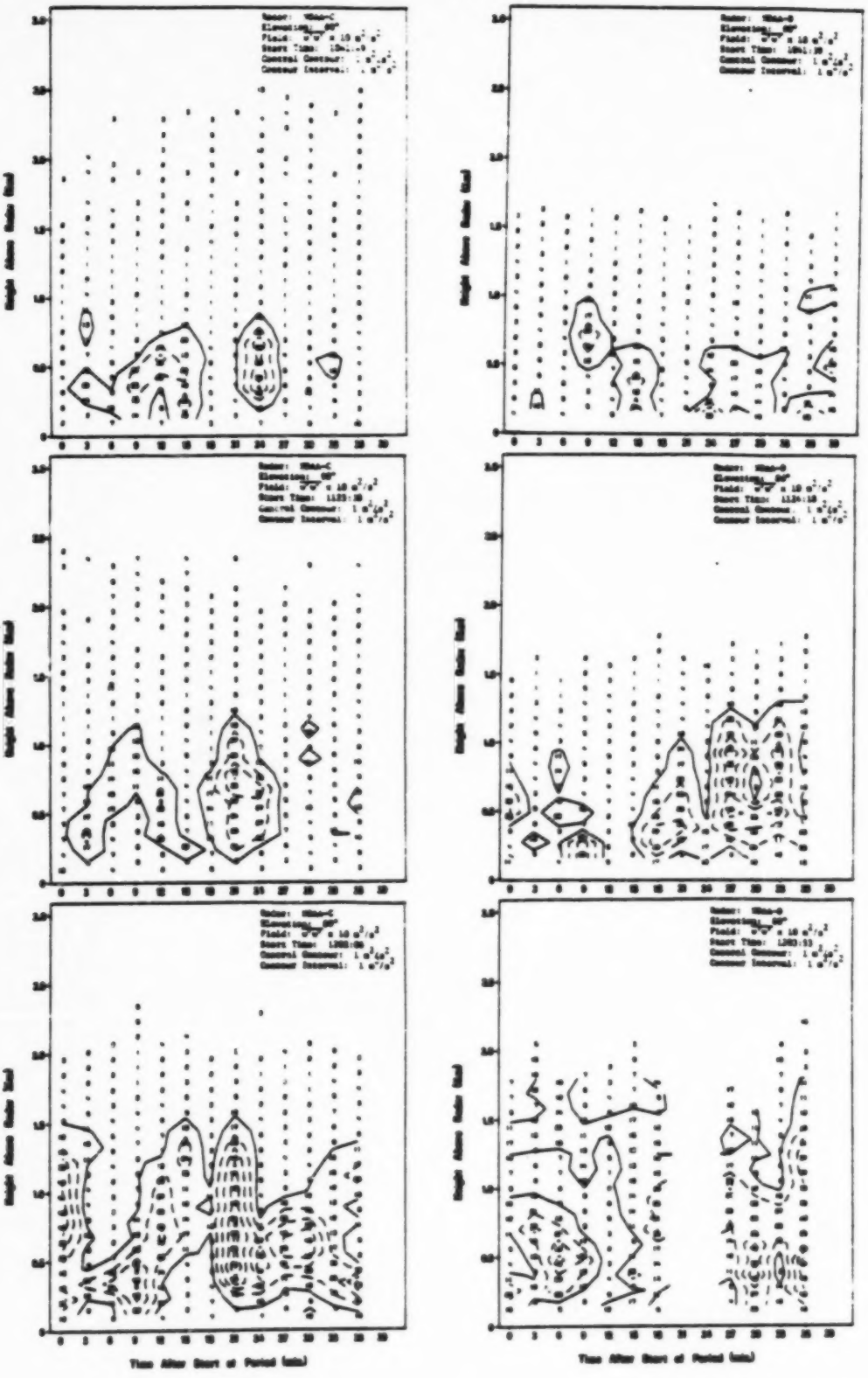

BEST COPY AVAILABLE

Vertical velocity variance profiles at 80°.

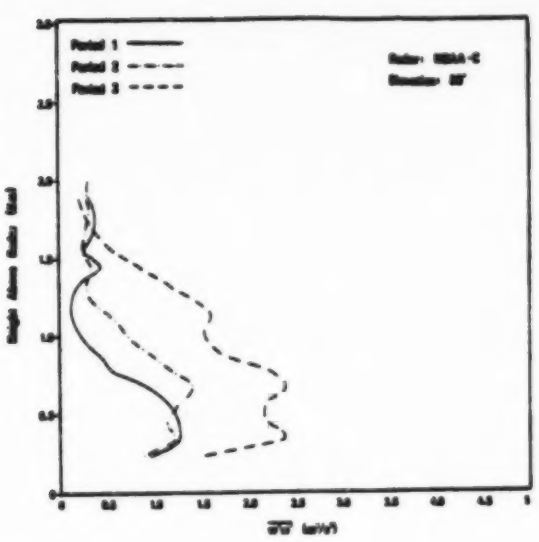

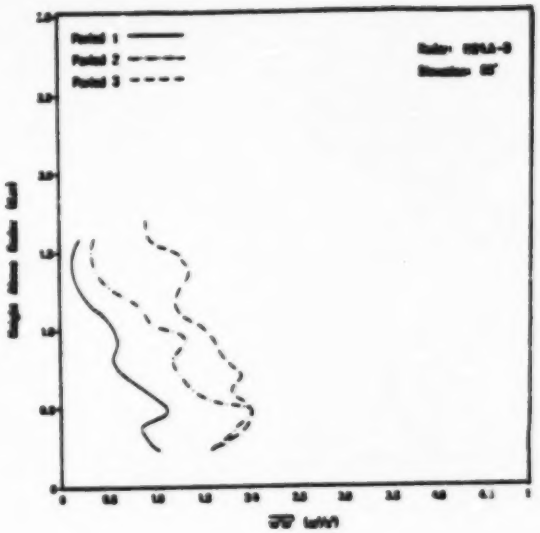

BEST COPY AVAILABLE